

TRMM Latent Heating Retrieval and Comparisons with Field Campaigns and Large-Scale Analyses

W.-K. Tao¹, Y. N. Takayabu²,
S. Lang^{1,3}, S. Shige⁴, W. Olson^{1,5},
A. Hou¹, X. Jiang^{6,7}, C. Zhang⁸, W. Lau¹, T. Krishnamurti⁹, D. Waliser⁶, M. Grecu^{1,5},
P. E. Ciesielski¹⁰, R. H. Johnson¹⁰, R. Houze¹¹, R. Kakar¹², K. Nakamura¹³,
S. Braun¹, S. Hagos⁸, R. Oki¹⁴, and A. Bhardwaj⁹

¹ *Mesoscale Atmospheric Processes Laboratory, NASA Goddard Space Flight Center,
Greenbelt, MD, USA*

² *Atmosphere and Ocean Research Institute, the University of Tokyo, Kashiwa, Chiba, Japan*

³ *Science Systems and Applications Inc., Lanham, MD, USA*

⁴ *Division of Earth and Planetary Sciences, Kyoto University, Kyoto, Japan*

⁵ *UMBC Joint Center for Earth Systems Technology, Baltimore, MD, USA*

⁶ *Jet Propulsion Laboratory, California Institute of Technology, Pasadena, CA, USA*

⁷ *Joint Institute for Regional Earth System Science & Engineering, University of California,
CA, USA*

⁸ *Rosenstiel School of Marine and Atmospheric Science, University of Miami, Miami, FL,
USA*

⁹ *Dept. of Meteorology, Florida State University, Tallahassee, FL, USA*

¹⁰ *Department of Atmospheric Science, Colorado State University, Fort Collins, CO, USA*

¹¹ *Department of Atmospheric Science, University of Washington, Seattle, WA, USA*

¹² *NASA Headquarters, Science Mission Directorate, Washington D.C., USA*

¹³ *Hydrospheric Atmospheric Research Center, Nagoya University, Nagoya, Japan*

¹⁴ *Earth Observation Research Center, Japan Aerospace Exploration Agency, Tsukuba,
Japan*

Multiscale Convection-Coupled Systems in the Tropics

AMS Meteorological Monograph in tribute to the late Professor Yanai

Due by October 6, 2012

Corresponding Author

Dr. Wei-Kuo Tao, NASA/Goddard Space Flight Center, Mesoscale Atmospheric Processes
Laboratory (Code 612), Greenbelt, MD 20771

Email: Wei-Kuo.Tao-1@nasa.gov

Abstract

Rainfall production is a fundamental process within the Earth's hydrological cycle because it represents both a principal forcing term in surface water budgets, and its energetics corollary, latent heating (LH), is one of the principal sources of atmospheric diabatic heating. Latent heat release itself is a consequence of phase changes between the vapor, liquid, and frozen states of water. The vertical distribution of LH has a strong influence on the atmosphere, controlling large-scale tropical circulations, exciting and modulating tropical waves, maintaining the intensities of tropical cyclones, and even providing the energetics of midlatitude cyclones and other mobile midlatitude weather systems. Moreover, the processes associated with LH result in significant non-linear changes in atmospheric radiation through the creation, dissipation and modulation of clouds and precipitation.

Yanai *et al.* (1973) utilized the meteorological data collected from a sounding network to present a pioneering work on thermodynamic budgets, which are referred to as the apparent heat source (Q_1) and apparent moisture sink (Q_2). Yanai's paper motivated the development of satellite-based LH algorithms and provided a theoretical background for imposing large-scale advective forcing into cloud-resolving models (CRMs). These CRM-simulated LH and Q_1 data have been used to generate the look-up tables used in LH algorithms.

This paper examines the retrieval, validation, and application of LH estimates based on rain rate quantities acquired from the Tropical Rainfall Measuring Mission satellite (TRMM). TRMM was launched in November 1997 as a joint enterprise between the American and Japanese space agencies -- with overriding goals of providing accurate four-dimensional estimates of rainfall and LH over the global Tropics and subtropics equatorward of 35°. Other literature has acknowledged the achievement of the first goal of obtaining an accurate rainfall climatology. This paper describes the second major goal of obtaining credible LH estimates as well as their applications within TRMM's zone of coverage, the standard TRMM LH products, and areas for further improvement.

1. Introduction

The release of latent heat during precipitation formation is of immense consequence to the nature of large- and small-scale atmospheric circulations, particularly in the Tropics where various large-scale tropical modes dominated by latent heating (LH) persist and vary on a global scale. Latent heat release and its variation are without doubt some of the most important physical processes within the atmosphere and thus play a central role in the Earth's water cycle.—The launch of the Tropical Rainfall Measuring Mission satellite (TRMM), a joint U.S.-Japan project, in November of 1997 made it possible for quantitative measurements of tropical rainfall to be obtained on a continuous basis over the global Tropics. TRMM has provided much-needed accurate measurements of rainfall as well as estimates of the four-dimensional structure of LH over the global Tropics. Over the last few years, standard LH products from TRMM measurements have become established as a valuable resource for scientific research and applications (see a review by Tao *et al.* 2006 and the papers published in the *J. of Climate* special collection on TRMM diabatic heating). Such products enable new insights and investigations into the complexities of convective system life cycles, diabatic heating controls and feedbacks related to meso- and synoptic-scale circulations and their prediction, the relationship of tropical patterns of LH to the global circulation and climate, and strategies for improving cloud parameterizations in environmental prediction models. TRMM's success provided the impetus for another major international satellite mission known as the Global Precipitation Measurement (GPM) to be launched by NASA and JAXA in 2014 (<http://gpm.nasa.gov>). As the centerpiece of NASA's Weather and Global Water/Energy Cycle research programs, GPM consists of a constellation of satellites provided by a consortium of international partners to provide the next-generation of spaceborne precipitation measurements with better sampling (3-hourly over a specific location), higher accuracy (with a Ku-Ka band radar), finer spatial resolution (up to 0.1° by 0.1°) and greater coverage (from the Tropics to high latitudes) relative to TRMM.

LH is dominated by phase changes between water vapor and small liquid or frozen cloud-sized particles. It consists of the condensation of cloud droplets, evaporation of cloud droplets and raindrops, freezing of cloud droplets and raindrops, melting of ice, snow and

graupel/hail, and the deposition and sublimation of ice particles. It is important to keep in mind that eddy heat flux convergence from cloud motions can also redistribute the heating or cooling associated with LH vertically and horizontally. LH cannot be measured directly with current techniques, including current remote sensing or in situ instruments, which explains why nearly all retrieval schemes depend heavily on some type of cloud-resolving model or CRM (Tao *et al.* 2006). However, the apparent heat source or Q_1 , of which LH is an important component, can be derived indirectly by measuring vertical profiles of temperature and the associated 2D wind fields from extensive rawinsonde networks through a residual method (known as a diagnostic heating budget, Yanai *et al.* 1973).

1.1 Radiosonde-based heating structures (Yanai *et al.* 1973)

Based on the residual approach, the composite diabatic heating profile of Q_1 can be derived indirectly over a spatial domain by measuring profiles of temperature, pressure, and the 2D wind field from a suitably spaced circumscribing network of radiosondes. This is called an “*apparent heat source*”, first described in the seminal papers by Professor Yanai (Yanai 1961 and Yanai *et al.* 1973), and expressed by:

$$Q_1 = \bar{\pi} \left[\frac{\partial \bar{\theta}}{\partial t} + \bar{V} \cdot \nabla \bar{\theta} + \bar{w} \frac{\partial \bar{\theta}}{\partial z} \right], \quad (1)$$

where $\bar{\pi}$ is the non-dimensional pressure, and the RHS is the total derivative of θ (times the non-dimensional pressure) measurable from radiosonde data. Here the large-scale vertical motion (w) is diagnosed from the 2D wind via the kinematic method with appropriate boundary conditions on w at the surface and the tropopause. There is an accompanying equation for the apparent moisture sink or drying (Q_2), which is similar to Eq. (1) except that $\bar{\theta}$ is replaced by water vapor specific humidity (\bar{q}) and Q_1 is replaced by negative Q_2 . In order to derive Eq (1), Yanai *et al.* (1973) stated that “*we consider an ensemble of cumulus clouds, which is embedded in a tropical large-scale motion system, then we imagine a horizontal area that is large enough to contain the ensemble of clouds, but small enough to be regarded as a fraction of the large-scale system.*”

Both the vertical velocity in the third term on the RHS and the horizontal and vertical advection terms on the RHS of the Eq. (1) have been used to force CRMs (or cumulus ensemble models) to study the response of convective systems to large and mesoscale processes (Soong and Tao 1980). This CRM approach to studying cloud and precipitation processes is called "*cloud ensemble modeling*" (Soong and Tao 1980; Tao and Soong 1986; Tao *et al.* 1987; Krueger 1988; Moncrieff *et al.* 1997; also see review papers by Tao 2003 and Tao and Moncrieff 2009). It allows many clouds of various sizes and stages to exist at any given time. The advantage is that modeled rainfall, Q_1 and Q_2 usually agree well with observations (Tao 2003; Randall *et al.* 2003; and others). The model results also include cloud statistics representing different types of cloud systems over their life cycle. Large-scale forcing derived from many field programs (e.g., GATE, TOGA COARE, SCSMEX, TWICE and others) have been used to drive CRMs. These CRM-simulated datasets are especially valuable for LH algorithm developers (see previous work by Tao *et al.* 1990, 1993, 2000, 2006, 2010; Shige *et al.* 2004, 2007, 2008, 2009; and Grecu and Olson 2006).

1.2 CRM-based heating structures

CRMs are one of the most important tools used to establish quantitative relationships between diabatic heating and rainfall. This is because LH is dominated by phase changes between water vapor and small, cloud-sized particles; these particles as well as their changes are difficult to detect directly using remote sensing techniques (though some passive microwave frequencies respond to path-integrated cloud water and CloudSat can detect such particles in the tops of clouds). CRMs, however, employing sophisticated microphysical schemes (that are by no means yet perfect) can explicitly simulate the conversion of cloud condensate into raindrops and various forms of precipitating ice. It is these different forms of precipitation that are most readily detected from space, and which ultimately reach the surface in the form of rain in the Tropics. CRMs have been used for TRMM for both rainfall and heating retrieval algorithm development.

Under the Boussinesq approximation, the heat (temperature) budget can be explicitly calculated by a CRM (e.g., Tao and Simpson 1989):

$$Q_1 - Q_R = \bar{\pi} \{ -(1/\bar{\rho}) [\overline{\partial \bar{\rho} w' \theta' / \partial z}] - \overline{\nabla \cdot V' \theta'} \} + (1/c_p) [L_v(c - e) + L_f(f - m) + L_s(d - s)], \quad (2)$$

where the primes indicate deviations from the large-scale environment due to smaller scale cloud processes. The variable θ is potential temperature, $\bar{\rho}$ is density, $\bar{\pi} = (p/P_{oo})^{R/c_p}$ is non-dimensional pressure (where p and P_{oo} are dimensional and reference pressures, respectively, with P_{oo} taken as 1000 hPa), and c_p and R are the specific heat of dry air at constant pressure and the gas constant of dry air, respectively. The variables L_v , L_f , and L_s are the latent heats of condensation, freezing, and sublimation, respectively, while the variables c , e , f , m , d , and s are the condensation of cloud droplets, evaporation of cloud droplets and rain drops, freezing of water droplets and rain drops, melting of ice crystals, snow flakes, graupel and hail, deposition of ice crystals, and sublimation of all ice hydrometeors, respectively. The term $(1/c_p) [L_v(c - e) + L_f(f - m) + L_s(d - s)]$ is defined as the LH due to microphysical phase changes while the first two terms on the RHS of Eq. (2) are the vertical and horizontal eddy heat flux divergence, respectively. The horizontal divergence term is neglected when Eq. (2) is spatially averaged over an area suitable for diagnostic analysis.

Figure 1 shows CRM-simulated time-domain mean profiles of heating/cooling due to the individual microphysical processes (i.e., condensation, evaporation, deposition, sublimation, melting, and freezing) in the convective and stratiform regions of a tropical MCS using the Goddard Cumulus Ensemble model (GCE, Tao and Simpson 1993). Condensation and evaporation have the largest magnitudes in the convective region with evaporation and sublimation about one-third the values of the condensation and deposition rates, respectively. Melting and freezing are small compared to condensation, evaporation, deposition, and sublimation; however, melting is responsible for converting precipitating ice to rain, which can then fall to the surface. Figure 2 shows vertical profiles of LH, vertical eddy heat flux divergence, radiation, and Q_I averaged over a 9-day period during SCSMEX over the northern enhanced sounding array (NESA). LH is the largest term in the Q_I budget via the heat released by condensation and deposition (as shown in Fig. 1). Its peak is around 6.5 km.

The radiative term (Q_R) accounts for about 1-3° of cooling per day. The eddy transport is the smallest term, but it does redistribute heat through cloud updrafts and downdrafts. The CRM-simulated Q_I profile is in very good agreement with the observed (i.e., Fig. 3 in Tao 2007).

2. LH retrieval algorithms

The primary TRMM instruments used to measure rainfall are the TRMM Microwave Imager (TMI), precipitation radar (PR), and the Visible and Infrared Scanner (VIRS, Kummerow et al. 1998; for additional details see <http://trmm.gsfc.nasa.gov>). Five different TRMM LH algorithms designed for applications with satellite-estimated surface rain rate and precipitation profile inputs have been developed, compared, validated, and applied in the past decade (see a review by Tao *et al.* 2006). They are the: (1) Goddard Convective-Stratiform Heating (CSH) algorithm, (2) Hydrometeor Heating (HH) algorithm, (3) Goddard TRAIN (Trained Radiometer) algorithm, (4) Spectral Latent Heating (SLH) algorithm, and (5) Precipitation Radar Heating (PRH) algorithm. Table 1 gives a summary of the five algorithms, including the type(s) of TRMM input data used to generate their associated heating product(s), the type of heating product(s) produced, and the salient reference(s) describing their design. Additional improvements made to the SLH, TRAIN and CSH algorithms as well as brief descriptions of the HH and PRH algorithms are presented next.

2.1 The SLH algorithm

Spectral representation of precipitation profiles obtained from the PR algorithm by use of a small set of distinct profile properties, as reported by Takayabu (2002), provide the basis for the SLH algorithm, which was introduced and modified by Shige *et al.* (2004, 2007, 2008, 2009). This algorithm is currently intended for use with PR-retrieved rain rate profiles only and estimates LH, $Q_I - Q_R$ and Q_2 . Akin to the CSH algorithm, a set of three look-up tables (LUTs) is produced using the GCE associated with three types of rainfall: (1) convective, (2) shallow-stratiform, and (3) anvil. Specifically, however, the LUTs are indexed according to vertical rain profile information: precipitation top height (PTH) for convective and

shallow stratiform rain and melting-level rain intensity for anvil (deep stratiform with a PTH higher than the melting level) rain. The nomenclature “spectral” stems from the spectrally-indexed table, designed to reduce the dependency on GCE/CRM simulations from specific field campaigns.

In the latest version of the SLH algorithm, deep stratiform rain is further divided into two new categories: deep stratiform with decreasing precipitation from the melting level toward the surface and deep stratiform with increasing precipitation from the melting level toward the surface (Shige *et al.* 2012, in preparation). It computes deep stratiform cooling magnitudes as a function of P_m (melting level) – P_s (surface rain rate), assuming the evaporative cooling rate below the melting level in deep stratiform regions is proportional to the reduction in the precipitation profile toward the surface from the melting level (based on 1D water substance conservation). However, increasing precipitation profiles are found in some portions of stratiform regions, especially in regions adjacent to convective regions where 1D water substance conservation may be invalid. An LUT¹ for deep stratiform with increasing precipitation toward the surface from the melting level is produced with the amplitude determined by P_s .

2.2 The TRAIN algorithm

The TRAIN heating algorithm is designed specifically for application with TMI passive microwave (PMW) radiance observations. First, precipitation and heating profiles are derived from PR reflectivity profiles, using a method similar to that of Shige *et al.* (2004), over a one-month span of PR observations. In this method, month-long CRM (i.e., GCE) simulations of precipitation/heating during SCSMEX (18 May - 17 June 1998), TOGA COARE (19 December 1992 - 18 January 1993) and KWAJEX (6 August - 5 September 1999) are used to relate vertical reflectivity structure and surface rain rate to vertical heating structure. Since TMI-observed microwave brightness temperatures (Tbs) are collocated with PR observations over the PR swath, TMI Tbs are assigned to each precipitation/heating

¹ It is based on four 9-day (10-18 December 1992, 27 December 1992 - 4 January 1993, 9-17 February 1993, and 18-26 February 1993) and one 8-day (19-26 December 1992) TOGA COARE CRM simulation.

profile in the large PR-derived database. The database then serves as a kind of LUT to be used in a Bayesian method to estimate precipitation and LH from the TMI. Given a set of TMI-observed Tbs, an estimated precipitation/heating profile is constructed by compositing database precipitation/heating profiles associated with Tbs that are consistent with the TMI-observed Tbs and their uncertainties.

Originally developed for application with SSM/I data, the Bayesian method was adapted for application with TMI radiances and integrated within the GPROF TMI precipitation retrieval algorithm (see Olson *et al.* 1999, 2006). Versions of the GPROF heating algorithm were used by Rodgers *et al.* (1998, 2000) to diagnose the relationship between LH distributions and storm intensification within Hurricane Opal and Supertyphoon Paka. More recently, Grecu and Olson (2006) and Grecu *et al.* (2009) demonstrated that Q_I profiles from TRAIN were consistent with independent estimates derived from SCSMEX and MISMO (the Mirai Indian Ocean cruise for the Study of the MJO convection Onset) rawinsonde analyses. Q_I was estimated by combining TRAIN estimates of Q_I - Q_R with Q_R estimates from the Hydrologic cycle and Earth Radiation Budget (HERB) algorithm of L'Ecuyer and Stephens (2003, 2007).

2.3 The CSH algorithm

Diagnostic budget studies (e.g., Houze 1982 and Johnson 1984) and cloud modeling studies (see review by Tao 2003) have shown that characteristic LH profiles in the stratiform regions of tropical MCSs are considerably different than the characteristic LH profiles in the convective regions. In general, for both observed and simulated convective systems, evaporative cooling in the lower troposphere below a bow-shaped positive heating profile in the middle and upper cloud layers (peaking in the middle to upper troposphere) is the dominant feature within stratiform precipitation regions (i.e., the archetypical reverse S-shaped stratiform LH profile), while a combination of vertically continuous condensation and deposition heating (peaking in the middle troposphere) is the dominant signature for convective rain areas (i.e., the archetypical, deep, all-positive, bow-shaped convective LH

profile). Based on these findings, the CSH algorithm was developed and described by Tao *et al.* 1993.

Recently, the CSH algorithm was re-designed and improved (Tao *et al.* 2010). The key difference between the new and old versions (Tao *et al.* 1993, 2000, 2001) involves the new LUTs² and how they are accessed. First, there are many more heating profiles (approximately 700 total compared to 20 in the previous version³) in the new LUT due to their being separated into detailed intensity and stratiform bins. And second, the profiles are distributed and thus accessed according to conditional rain rates. Together these lead to several potential advantages regarding heating structure. Obviously, having many more profiles in the LUT allows for the possibility of having many more heating structures. For example, rather than just having shallow (i.e., < 5 km) or deep heating profiles, the new LUT allows the depth of heating to vary considerably⁴. Using conditional rain rates is what allows those structures to be better differentiated. For example, given a stratiform fraction and an average rain rate over a region (i.e., a 0.5° x 0.5° area), knowing that average rain rate is due to a small area of intense rain (e.g., a single intense convective cell) rather than a larger area of weak rain (e.g., a broader field of weaker convective cells) allows the algorithm to select a more representative heating structure. In the older version, these two rain areas would have been treated the same. The newer LUTs include CRM-generated LH, eddy heating and radiative heating/cooling at common levels on a common grid. They can

² To date, field program data that have been examined in conjunction with the CSH algorithm include: (1) GATE (the Global Atmospheric Research Program's Atlantic Tropical Experiment), (2) EMEX (the Equatorial Monsoon Experiment), (3) PRE-STORM (the Preliminary Regional Experiment for STORM-Central), (4) TOGA COARE (the Tropical Ocean Global Atmosphere – Coupled Ocean Atmosphere Response Experiment), (5) SCSMEX (the South China Sea Monsoon Experiment), (6) TRMM-LBA (TRMM Large-Scale Biosphere-Atmosphere Experiment), (7) KWAJEX (the Kwajalein Experiment), and (8) DOE-ARM (the Department of Energy Atmospheric Radiation Measurement Program).

³ These profiles were obtained by distributing heating/cooling profiles from model sub-domains (64 km or the approximate grid size of the TRMM rain retrievals) into the same conditional rain intensity and stratiform percentage bins used to differentiate the surface rainfall distributions. Separate LUTs were constructed for each of the three main components: latent, eddy (horizontal and vertical combined) and radiative.

⁴ Mean echo top heights from the PR and from the model correlate nicely over almost the entire range of LUT bins (not shown).

thus easily provide the eddy and radiative terms to other LH algorithm groups⁵ (at the same rainfall intensity and stratiform percentage).

2.4 *The HH and PRH algorithms*

Neither the HH nor the PRH algorithm use pre-calculated LH profiles in LUTs. Instead, both schemes estimate the net flux of water mass into (out of) layers and assume that under steady-state conditions net fluxes are compensated for by a local decrease (increase) of hydrometeors by microphysical processes. Thus, a decrease in mass is associated with evaporation, melting, or sublimation cooling, whereas an increase is associated with condensation, freezing, or deposition heating.

The HH algorithm, including its verification and global application, is described in Yang and Smith (1999a-b, 2000). These studies describe how cloud-scale vertical velocity can be estimated using multiple-linear regression based on hydrometeor profile densities as independent input variables. For applications with TRMM level 2 retrievals, the current scheme uses truncated Legendre polynomial representations of precipitation mass fluxes from the surface to precipitation top height (PTH) before taking vertical derivatives, thus preventing retrieval noise from producing unrealistic heating rates. For applications with PR data, no account is made for LH by deposition-sublimation and freezing-melting above and below the melting level since the sensitivity of the PR is only 17 dBZ, which is insufficient for detection of most frozen precipitation, particularly for small and/or less dense graupel particles. For applications with TMI data, terminal velocities of precipitating rain and graupel are calculated assuming that both size spectra are distributed according to a Marshall-Palmer distribution.

The PRH algorithm uses PR-based retrievals (precipitation profiles and convective/stratiform rain classification) to estimate the vertical LH structure (Satoh and Noda 2001). It requires an initial-guess vertical velocity profile that is used to evaluate a hydrometeor conservation

⁵ Since the various algorithms produce different heating, it was recommended by the TRMM Latent Heating Working Group at the 5th TRMM LH workshop (Annapolis, Maryland, 27-28 August 2007) that CSH should provide the eddy and radiative terms to the other algorithms.

equation under steady state conditions. In stratiform regions, the LH profile is derived directly from the hydrometeor conservation equation (similar to the HH algorithm). In convective regions, if a net increase of hydrometeors due to microphysics is inferred from the conservation equation, then the associated LH profile is calculated based upon the vertical motion profile, assuming saturated adiabatic ascent. An iterative method is then used to adjust the original vertical motion profile to ensure that the vertically integrated net heating and surface rain rate are consistent.

3. Field campaigns and validation

As discussed in section 1, advective forcing in temperature and water vapor have been used as forcing for CRMs to simulate cloud and precipitation properties including LH, Q_I and Q_R for TRMM LH algorithm developers. These simulated LH profiles including their convective and stratiform components and their relationship to surface rainfall have been used to generate LUTs for LH algorithms. In addition, these simulated data and their associated observed Q_I have been used for validation. This section briefly describes the GCE model simulations, field data used and validation of LH algorithms.

3.1 Field campaign sites

SCSMEX was conducted in May-June 1998. Two major convective events, prior to and during monsoon onset (18-26 May 1998) and post monsoon onset (2-11 June 1998), were observed. The SCSMEX forcing data were obtained from a variational analysis approach (Zhang and Lin 1997; Zhang *et al.* 2001) and used to drive the GCE for 44 days starting at 0600 UTC 6 May 1998. TOGA COARE was conducted from November 1992 through February 1993 over the central Pacific. The most intense convection during TOGA COARE occurred in mid and late December 1992, prior to the peak in a westerly wind burst around 1 January 1993. Several major convective events occurred around 11-16 and 20-25 December 1992, mainly due to the low-level large-scale convergence of easterlies and westerlies (Lin and Johnson 1996). For TOGA COARE, the large-scale forcing used in the GCE was derived from the intensive flux array (IFA) sounding network (Ciesielski and Johnson 2003).

GATE was conducted in 1974 over the East Atlantic. Cloud systems (non-squall clusters, a squall line, and scattered convection) for the period 1-8 September 1974 during phase III of GATE have also been simulated using the GCE (Li *et al.* 1999; Tao 2003). Large-scale GATE forcing from Sui and Yanai (1986) were used to drive the GCE. The environmental conditions for SCSMEX, TOGA COARE and GATE can be found in Tao *et al.* (2004). The TOGA COARE surface flux algorithm (Fairall *et al.* 1996) was used to calculate sea surface fluxes for these oceanic cases.

KWAJEX was sponsored by NASA in cooperation with the U.S. Army Kwajalein Atoll/Kwajalein Missile Range and the National Oceanographic and Atmospheric Administration (NOAA) and was conducted from 23 July to 15 September 1999. It was designed to obtain an empirical physical characterization of precipitating convective clouds over the tropical ocean and to improve physical assumptions made within the TRMM satellite algorithms. TRMM LBA took place in Amazonia in Brazil and focused on the dynamical, microphysical, electrical and diabatic heating characteristics of tropical convection in the region. Diagnostic analyses from sounding data for KWAJEX and TRMM LBA are reported in Schumacher *et al.* (2007). TWP-ICE was a comprehensive observing campaign around Darwin, Australia to study weather and climate change through improved understanding and modeling of cloud and aerosol processes in tropical cloud systems (May *et al.* 2008). The GCE has been used to study convective systems from LBA (Lang *et al.* 2007, 2011), TWP-ICE (Zeng *et al.* 2010, 2012) and KWAJEX (Zeng *et al.* 2008, 2009a,b, 2011). Table 2 shows the location, duration and references for the various field campaigns.

The ARM program established the SGP site to observe clouds and precipitation for climate research. The site is centered at 36.6°N, 96.5°W. Two summer field campaigns were conducted at the site in 1997 and 2002 and are referred to here as ARM-SGP-97 and -02. The ARM forcing data were also obtained from the variational analysis approach of Zhang and Lin (1997) and Zhang *et al.* (2001). Surface fluxes taken from site-wide averages of observed fluxes from the ARM Energy Balance Bowen Ratio (EBBR) stations are imposed into the model (Zeng *et al.* 2007, 2011). The ARM-SGP-97 numerical simulation starts at 2330 UTC 18 June 1997 and lasts for 29 days. The ARM-SGP-02 simulation starts at 2030

UTC 25 May 2002 and lasts for 20 days. For the ARM cases, the surface wind does not interact with the boundary layer.

Table 3 shows grid-averaged total rainfall and stratiform rain percentage for each of the GCE-simulated cases. The oceanic cases have more rainfall than the continental. This is due primarily to the fact that the oceanic environments have higher precipitable water contents (i.e., more moisture) than the continental (see Table 1 in Tao *et al.* 2004). That is why the SCSMEX simulation has the largest rainfall amount. Although the TOGA COARE environment is generally moister than that for GATE, it has less rainfall because the model simulation starts in November, which did not have many active convective events. In general, the tropical oceanic cases should have a higher stratiform amount (i.e., 40-50%) than the midlatitude continental cases. However, the ARM cases also have a large stratiform rain fraction (from 36 to 41%) because they include frontal cases. Houze (1977), Zipser *et al.* (1981) and Gamache and Houze (1983) estimated that widespread stratiform rain accounted for about 32%-49% of the total rainfall during GATE. The fraction of stratiform rainfall from midlatitude squall lines has been estimated at 29%-43% (Rutledge and Houze 1987; Johnson and Hamilton 1988). The GCE-simulated results are in good agreement with these observations. Figure 3 shows the geographic locations of field campaigns used to provide data to drive and evaluate CRM simulations.

3.2 Validation of LH algorithms

Validation of LH profiles retrieved from satellite data is not straightforward because there is no instrument (i.e., no “*latent heatometer*”) or direct means to measure this quantity, and as a result, there is no primary calibration standard by which the validation process can be adjudicated. Two methods, consistency checks using CRMs and comparisons with diagnostic budget estimates, have been used for validation.

(a) Comparison of CRM heating with reconstructed and diagnostic heating

Consistency checks involving CRM-generated heating profiles and both algorithm-reconstructed and diagnostically-estimated heating profiles are a useful step in evaluating the performance of a given LH algorithm. In this process, as time-varying CRM-simulated precipitation processes (multiple-day time series) are used to obtain the required input parameters for a given LH algorithm, the algorithm can then be used to reconstruct the actual heating profiles within the CRM simulation using various model quantities (e.g., surface rainfall) as pseudo observations from the model. Finally, both sets of conformal estimates (model and algorithm) can be compared to coincident estimates of diagnostically-based heating derived from radiosonde observations. Such observations from various field experiments, as well as simulations of individual precipitation systems, have been used for such consistency checks (Tao *et al.* 1990, 1993, 2000; Olson *et al.* 1999, 2006; Shige *et al.* 2004, 2007, 2008).

It is evident in Fig. 4 that the temporal variations of both the CSH- and SLH-reconstructed LH profiles are generally similar to the variations in the GCE simulation profiles. For example, both capture the evolution of a quasi-2-day oscillation, which occurred during the period 1800 UTC 23 - 1800 UTC 25 December 1992, an oscillation earlier noted by Takayabu *et al.* (1996). However, as pointed out by Shige *et al.* (2004), there are noteworthy improvements in the SLH-reconstructed profiles for the shallow-convective stage from 1800 UTC 23 to 0600 UTC 24 December 1992 and in the anvil decay stage from 0600 UTC to 1800 UTC 25 December 1992. Shallow convective heating is more explicitly retrieved by the SLH algorithm because it uses observed information on precipitation depth (i.e., the PTH or precipitation top height parameter), and heating profiles in the decaying stage without surface rain (e.g., 1200 UTC 25 December) can be retrieved by the SLH algorithm by using the precipitation rate at the melting level. Both the CSH- and SLH-reconstructed results are smoother than the GCE simulations because the associated LUTs contain averaged profiles for each height/rain bin.

(b) *Comparison of satellite-retrieved heating with diagnostically-calculated heating*

One of the TRMM field campaigns, SCSMEX, which included two sounding networks, the NESA (northern enhanced sounding array) and SESA (southern enhanced sounding array), was conducted in May and June 1998. One of the main underlying scientific objectives of the experiment was to help validate TRMM precipitation and LH algorithms (*i.e.*, vertical profiles of multi-hydrometeor densities, rain rates, and LH). Diagnostic Q_I calculations based on the sounding networks were provided by Professor Richard Johnson at Colorado State University (Johnson and Ciesielski 2002; Ciesielski and Johnson 2006).

Two examples of validation results are presented in Fig. 5 for the SCSMEX NESA and SESA regions. These diagrams illustrate space/time-averaged vertical profiles of different heating terms obtained from the five different algorithms (*i.e.*, Q_I from CSH, LH from HH, Q_I and Q_I-Q_R from TRAIN, Q_I-Q_R and LH from SLH, and LH from PRH). In addition, the sounding-diagnosed (DIAG) mean Q_I profile produced by CSU is shown for comparison. For NESA, the results indicate that: (1) only SLH exhibits close agreement with the diagnostic (*i.e.*, DIAG) altitude of peak heating, (2) CSH, SLH, and TRAIN show close agreement with each other between low and middle levels, (3) CSH, HH, TRAIN, and PRH exhibit close agreement in the altitude of peak heating amongst themselves, and (4) all satellite algorithms except HH exhibit relatively close agreement in amplitude of peak heating amongst themselves, whereas HH exhibits considerably larger amplitude. In the case of SESA, the results indicate that: (1) HH and TRAIN exhibit very close agreement with each other in terms of level of peak heating, (2) CSH exhibits close and SLH very close agreement with the DIAG amplitude of peak heating, although the DIAG peak heating layer is somewhat broader aloft than either those of CSH or SLH (or any algorithm), (3) HH is the only algorithm to exhibit positive upper-level heating similar to DIAG, but it also exhibits the largest amplitude of peak heating relative to the other algorithms, (4) Q_R -augmented TRAIN's Q_I term exhibits the smallest amplitude of peak heating relative to the other algorithms, (5) PRH's lower-level heating agrees well with DIAG and (6) all of the other algorithms except TRAIN Q_I have small low-level heating. It should be noted that in addition to the algorithms themselves, differences between the retrieved and observed profiles could also arise from insufficient satellite sampling of the budget domain both in space and time. The inconsistency of the physical quantities of the results (*i.e.*, having

different heating products from different heating algorithms) must also be resolved in future intercomparisons.

Table 4 lists the altitude of maximum mean heating for the algorithm retrievals and the diagnostic calculations including other cases from a validation study. For all algorithms except HH, the stratiform percentage is needed as a crucial term in determining the respective altitude of peak heating. Generally, a greater stratiform percentage is associated with a higher altitude of maximum heating. For the HH algorithm, which derives its LH profile from the vertical derivative of total rain mass flux adjusted by any cloud layer lift or descent, its level of peak heating is largely determined by the height at which the rain mass flux begins to decrease upward. For several cases, the altitudes of maximum mean heating for the algorithms are within 1 km of the diagnostic peak heating levels. However, greater departures are also found, particularly for the less robust KWAJEX case⁶ in which the diagnostic calculation indicates a 4.5 km level of maximum heating. Future work will be required to determine if this seemingly low altitude for maximum heating is actually realistic or a bias in the KWAJEX diagnostic analysis. In addition to mean profiles, CFADs (contoured frequency with altitude diagrams, Yuter and Houze 1995) are another useful way to validate LH profiles by comparing heating PDFs.

4. Applications of LH products

A special collection on TRMM diabatic heating was published in the *J. of Climate*; it is comprised of papers that derive, test, and compare different diabatic heating products derived from TRMM data. These papers highlight the challenges in separating contributions from deep convective, stratiform, and shallow convective clouds in using TRMM-derived products to study the distribution of diabatic heating and its impact on atmospheric circulations in the Tropics. In addition, some of these papers have compared the diabatic heating between sounding-estimates, large-scale model analyses and TRMM products. Table 5 lists the authors and titles of the papers published in this special collection. In this section, some of the applications of TRMM heating data are highlighted from these papers.

⁶ KWAJEX had a relatively low ratio of satellite sampling relative to the sounding array.

4.1 Shallow and deep latent heating modes and the large-scale circulation

Utilizing Q_I - Q_R data estimated from the SLH algorithm, Takayabu *et al.* (2010) showed that non-drizzle precipitation over tropical and subtropical oceans consists of two dominant modes of rainfall systems: deep systems and congestus. They found that while rain from congestus simply increases with sea surface temperature (SST), the deep convective precipitation is inhibited by large-scale atmospheric subsidence even though SSTs are warm enough to support congestus. Figure 6 compares Q_I - Q_R at 7.5 km and 2 km: the former represents the effect of deep organized precipitation, while the latter represents the effect of congestus rain. Over the central-to-eastern Pacific, in the southern hemisphere, along the equator, and also near the Hawaiian islands, for example, the congestus rain distribution neatly follows the SST distribution, even where deep convective rain is almost completely suppressed. Curiously, the congestus rain distribution, but not the deep convective, looks like a so-called double ITCZ, which had bothered climate model scientists for a long time.

Figure 7 shows 7-year mean Q_I - Q_R profiles over 30°N-30°S for September-November stratified against 500hPa vertical velocity. The results confirm the existence of two dominant modes in tropical non-drizzle precipitation and an effective suppression of the deep mode associated with large-scale subsidence, which is accompanied by middle to lower tropospheric drying. These results are in concert with the strong relationship between mid-to low-level tropospheric relative humidity and precipitation over the tropical oceans as indicated by Sherwood *et al.* (1999) and Bretherton *et al.* (2004). CRMs have been used to show that the entrainment of dry air in the lower to middle troposphere reduces the buoyancy of a cumulus cloud (e.g. Takemi *et al.* 2004; Takayabu *et al.* 2006). When the environmental air is very dry, the reduction of buoyancy is enough to prevent cumulus from penetrating above the freezing level. Were the cumulus convection able to penetrate the freezing level, it would gain additional buoyancy via the release of latent heat by freezing (Zipser 2003). This is why the development to deep convection is discretized at midlevels.

More recently, Hirota *et al.* (2010) compared the distributions of tropical precipitation from 19 models as part of CMIP3 (the Coupled Model Intercomparison Project phase 3) and found

that the double intertropical convergence zone (ITCZ) problem is linked to the cumulus convection scheme: the more sensitive the deep convective scheme is to mid-tropospheric humidity, the less problem there is with double ITCZs. This result is consistent with Del Genio *et al.* (2012) who attributed successful MJO model simulations to adequate representation of deep convection in relation to the mid-tropospheric humidity. Hirota *et al.* (2010) showed that the double ITCZ problem is absent in MIROC5, the current version of the climate model developed by the Atmosphere and Ocean Research Institute, National Institute for Environmental Studies, and the Japan Agency for Marine-Earth Science and Technology (AORI/NIES/JAMSTEC). This is attributable to a new entrainment scheme introduced by Chikira and Sugiyama (2010) to the cumulus parameterization. The essential impact of cumulus entrainment on deep precipitation is further examined by Hirota *et al.* (in preparation) in a sensitivity study utilizing the atmospheric part of MIROC5 that involves the cumulus entrainment rate parameter. It was confirmed that the entrainment rate controls the double ITCZ even for the same SST distribution. These results explain why congestus heating exhibits a double ITCZ-like distribution, while the deep heating does not.

4.2 *Rain and cloud characteristics and LH profiles during different phases of the MJO*

As a dominant sub-seasonal mode of tropical atmospheric variability, the Madden-Julian Oscillation (MJO, Madden and Julian 1971, 1994) exerts a pronounced influence on global climate and weather systems (see reviews by Lau and Waliser 2011; Zhang 2005) and is the primary source of predictability on sub-seasonal time scales (i.e., Waliser 2005; Gottschalck *et al.* 2010). In order to interpret the essential observed features of the MJO, prevailing MJO theories emphasize instability arising from various feedbacks between diabatic heating and large-scale dynamics, for example, from coupling between convective heating in the free atmosphere and Kelvin waves (e.g., “wave-CISK” or conditional instability of the second kind, Lau and Peng 1987; Chang and Lim 1988) or due to LH in the planetary boundary layer (PBL) by frictional moisture convergence (Wang and Rui 1990; Hendon and Salby 1994; Maloney and Hartmann 1998). In addition, the importance of higher-order vertical heating modes for MJO instability is emphasized (e.g., “stratiform instability”, Mapes 2000). Besides

convective heating, the role of radiative heating for the MJO is also proposed (e.g., Lin and Mapes 2004; Stephens *et al.* 2004; Masunaga *et al.* 2005).

Lau and Wu (2010) utilized TRMM observations to examine the characteristics of clouds, rainfall and LH associated with the eight MJO phases defined by the real-time multivariate Wheeler-Hendon index (Wheeler and Hendon 2004; hereafter WH index). They constructed a 2D cloud-rain probability distribution function (PDF) using Tb and echo top height (ETH) from all data points within the region (10°S–10°N, 120°–150°E) for the mean of all active phases as well as for each phase (Fig. 8). A bimodal distribution with an abundance of warm-low and cold-middle cloud and rain types is evident for all active (amplitude of WH index >1) phases of the MJO (Fig. 8a). The highest population is from the warm-low type, with Tbs warmer than 273 K and ETHs below the freezing level, which is climatologically located at approximately 5 km in the Tropics. The cold-middle type, identified as congestus, has a high population centered rather narrowly near the melting level with a wide range of cloud tops colder than 273 K. Four main regimes—WL (warm-rain low-level cloud), MM (mixed-phase rain, middle-level cloud), CM (cold cloud-top and medium storm height), and CH (cold rain, high-cloud)—are defined based on the Tb and ETH and are consistent with the four tropical precipitation systems—shallow, cumulus congestus, deep stratiform, and deep convective—classified in the observational study of Masunaga *et al.* (2005). In addition to these four regimes, the mean PDF of the MJO active cycle also shows a non-negligible warm rain, middle-level cloud (WM) regime, which counts for about 9% of the total population.

To focus on the changes in rain characteristics over the MJO life cycle, anomalous PDFs defined as the deviation of the PDF at a particular phase from that of the mean are shown in (Figs. 8b-i). During the early build-up stage (i.e., phases 1 and 2), there is an abundant occurrence of the WL type (color shaded), coupled with a large deficit in the MM and CM types (black and white contours). Between phase 2 and phases 3 and 4, the PDF switches from a bottom-heavy to a top-heavy distribution, with a large increase in MM and CM types representing an increase in mixed-phase precipitation with medium ETH. This corresponds to the second stage of build up when deep convection is developing. At phase 5, which

coincides with the maximum large-scale organization, the CM and CH types increase considerably, with most of the enhanced activity (color shaded) taking place at temperatures below 273 K, indicating the presence of mixed-phase and ice-phase precipitation. A broadening of the ETHs implies that shallow, middle, and deep convection are present at the same time. However, some shallow or middle clouds may not be counted in the presence of high stratiform clouds as a result of cloud layering effects. In phase 6, deep convection diminishes somewhat, with the convective system dominated by CM and MM types and with the presence of both precipitating and non-precipitating high-level anvil clouds associated with mature and decaying convection. Phase 7 signals the decaying stage, where a substantial amount of rain still comes from deep convective systems with ETHs above 6–7 km while at the same time, low-level rain reappears. By phase 8, the PDF has a structure similar to phase 1, indicating the completion of an MJO cycle with the WL-type rain reestablishing itself. Table 6 shows the main characteristics of each MJO phase in terms of Tb, ETH, and cloud system type.

Figure 9 shows mean TRMM daily LH profiles⁷ as well as the anomalous heating during the eight phases of the MJO cycle. Contributions from heating with ETHs less than and greater than 5 km are shown separately to demonstrate the relative contributions from shallow (liquid-phase and mixed-phase rain) and deep (ice-phase and mixed-phase rain) convection. The magnitude of the mean heating by shallow convection is about 30%–35% of that due to deep convection. Anomalous heating profiles (Figs. 9b-i) at each MJO phase are defined by the deviation from the mean profile. In phase 1, anomalous lower tropospheric heating is due to shallow convection ($\text{ETH} < 5 \text{ km}$) as well as by low-level moist processes associated with deep convection ($\text{ETH} > 5 \text{ km}$). In phase 2, both shallow and deep convection contribute about equally to the low-level heating. A switch from a bottom-heavy (warm and shallow convective rain) to a top-heavy (mixed convective and stratiform rain) heating profile occurs from phases 2 through 4, consistent with the PDF distributions shown previously. Note that the anomalous low-level heating from shallow convection in phase 3 is most likely from the abundant mixed-phase rain at this stage. During phases 4 and 5, the heating profiles show a

⁷ Prototype CSH-derived LH was used for this study because the new CSH algorithm was not available at that time.

dipole structure with maximum heating at about 7–8 km and cooling below 2–3 km, typical of that associated with stratiform rain systems (Houze 1989; Tao *et al.* 2006; Jakob and Schumacher 2008). The decaying phase shows almost a mirror image in the heating profile relative to the build-up phase. In phase 6, mid- and upper-tropospheric heating diminishes and low-level heating reverses sign, reflecting the reduction in warm-rain processes in the decaying phase. The reduction in liquid-phase rain processes continues in phases 6 and 7, with the deep heating profiles changing sign in the latter. Phase 8 completes the MJO cycle, with a large reduction in deep heating and the beginning of low-level heating processes. Even though the contribution to total heating by shallow convection is relatively small compared to deep convection⁸, the shallow convection and associated warm rain may be important in the regulation of moisture, clouds, and SST, especially during the build-up phase of the MJO.

4.3 *Comparing TRMM algorithm, sounding and reanalysis estimates of latent heating profiles over the Tropics*

Our knowledge on vertical structures of tropical diabatic heating is limited. Vertical structures of diabatic heating from numerical models, including data assimilation products, are strongly influenced by cumulus parameterization, a significance source of model error and uncertainty. Observational (indirect) estimates of diabatic heating profiles in the form of Q_1 using radiosonde data (Yanai *et al.* 1973) or radar data (Mapes and Houze 1995; Mather *et al.* 2007; Schumacher *et al.* 2008) from field campaigns are rare and do not provide a global perspective on the long-term means and variability of vertical diabatic heating structures. On the other hand, heating profiles from TRMM retrievals or data assimilation products provide global and long-term coverage. Their reliability must be quantitatively assessed for their proper application. Comprehensive comparisons of heating profiles representing large-scale vertical structures of diabatic heating in the Tropics from radiosondes, TRMM, and global reanalyses are summarized in this section. Their similarities and disagreement define an uncertainty envelope of our current knowledge of diabatic heating. Discussions cover mean profiles at field campaign sounding sites, global averages,

⁸ The new CSH-derived heating (V2) has more low-level heating compared to previous CSH-derived heating (see Fig. 10 in Tao *et al.* 2010).

temporal variability, and their dynamical implications.

4.3.1 Data

Time series of Q_I estimated from radiosonde observations are available from eight field campaigns (Table 2). All data represent averages over areas of roughly $10^3 - 10^5 \text{ km}^2$ in different tropical climate regimes (Fig. 3), including open ocean with only small or no islands (GATE, TOGA-COARE, KWAJEX and MISMO), coastal and monsoon regions (SCSMEX, TWP-ICE), and continental rainforest (LBA). Common to all locations are MCSs, such as squall lines, and the diurnal cycle. The time interval of all Q_I data is 6 h while the vertical levels range from 1000 to 100 hPa with a 25-hPa increment. All data are single time series. The TOGA COARE data were from the IFA. The GATE data are gridded ($1^\circ \times 1^\circ$), and a $3^\circ \times 3^\circ$ domain average covering the B-scale ship array was used in these studies.

Estimates of diabatic heating associated with precipitation and total diabatic heating were made from several global re-analyses, including three recently released high-quality reanalysis datasets (i.e., ERA-I, MERRA, and CFSR) as well as earlier reanalysis datasets (i.e., NCEP-II, JRA25, and ERA-40)⁹. All reanalysis products overlap with TRMM from 1 January 1998 to 31 December 2007. For all re-analyses, diabatic heating was estimated as Q_I from the 3D wind and temperature fields. CFSR and MERRA provide direct output of total diabatic heating (Q_T)¹⁰.

The TRMM heating products are available only in regions with precipitation (and hence are predominantly LH). When compared to the TRMM heating retrievals, diabatic heating from the re-analyses is set to zero if there is no precipitation. The focus in this section is the vertical structure of diabatic/LH in the Tropics, not its actual magnitude and spatial

⁹ ERA-I is the European Centre for Medium-Range Weather Forecasts (ECMWF) interim reanalysis (Dee *et al.* 2011), MERRA is the NASA Modern Era Retrospective Analysis for Research and Applications (Rienecker *et al.* 2011), CFSR is the National Centers for Environmental Prediction (NCEP) Climate Forecast System Reanalyses (Saha *et al.* 2010), NCEP-II is the NCEP–Department of Energy (DOE) reanalysis (Kanamitsu *et al.* 2002), JRA25 is the Japanese 25-year reanalysis (Onogi *et al.* 2007), and ERA-40 is the 40-year ECMWF reanalysis (Uppala *et al.* 2005).

¹⁰ Q_T is the total diabatic heating directly output from reanalyses as a component of the temperature tendency. Q_I is calculated as the residual of the heat budget.

distributions. The profiles presented here are sometimes normalized. For comparison, the TRMM products are re-gridded onto the ($2.5^\circ \times 2.5^\circ$) horizontal re-analysis grids and interpolated onto 17 re-analysis pressure levels. In comparing heating profiles from the soundings with those from the TRMM and re-analysis products, one should bear in mind that the estimates from the TRMM and re-analysis products are either purely LH (PRH) or diabatic heating only when there is precipitation (SLH, CSH, TRAIN, NCEP2, JRA25, ERA-40, and MERRA), while those from the soundings are purely total heating. But, diabatic heating profiles from the soundings include clear-sky points, which presumably do not contribute much to the total heating and hence have little impact on the normalized profiles of the total heating. For brevity, however, all the variables (Q_T , Q_I ¹¹, and LH) are referred to as diabatic heating.

4.3.2 General characteristics

Several tropical precipitation regions (Fig. 10) were defined to facilitate discussions on regional heating characteristics. Global time means of tropical diabatic heating profiles can be perceived as averages over these regions (with LH dominating, suitable for TRMM retrievals) or the entire Tropics (with both latent and radiative heating from the re-analyses). Mean profiles averaged over the precipitation regions reveal that the largest disagreement among the TRMM retrievals and re-analyses is low-level heating. Some products (e.g., SLH, TRAIN, NCEP2, MERRA, and JRA25) exhibit distinct or even dominant heating peaks below the 700 hPa level, which are very weak or absent in others (Fig. 11). Another related disagreement is the number of heating peaks in the vertical. Some products show two or more peaks (e.g., SLH, TRAIN, MERRA, and JRA25), others only one. These two major disagreements among the TRMM retrievals and re-analyses can be repeatedly seen in various comparisons with different configurations. Global zonal mean heating profiles from the re-analyses agree with each other well in their descriptions of the contrast between the Tropics and extratropics and between the oceans and land (Fig. 12). However, large disagreement in their heating peaks, either the level or the number, is obvious.

¹¹ Q_r is relatively small in regions of large precipitation.

Another way to characterize the heating profiles is to compare them as functions of the precipitation rate. In the Atlantic region, for example, TRMM and re-analysis estimates, except PRH, show their heating peaks becoming elevated as the precipitation rate increases (Fig. 13). This relationship between the LH profiles and the precipitation intensity is in agreement with the results of Short and Nakamura (2000), which showed a correlation of 0.71 between PR ETH and conditional rain rate over the Atlantic and eastern Pacific Oceans. The increase in heating peak with rain rate is gradual in some products (e.g., SLH, TRAIN, and MERRA) but fast or even abrupt in others (e.g., CSH, ERA40, JRA25). Double peaks exist at certain rain rates in PRH, ERA40, and JRA25. The only estimates that produce stratiform cooling in the lower troposphere at high precipitation rates are PRH and TRAIN. A similar diagnostic is performed over Africa (Hagos *et al.* 2010; not shown). There is no low-level heating peak in any of the three TRMM estimates (TRAIN has no estimate of heating over land). In the low precipitation rate tail, the TRMM estimates have elevated heating and low-level cooling. In the re-analysis estimates, there is an abrupt transition in the diabatic heating profiles with sensible heat fluxes and radiative cooling dominating below about 1 mm day^{-1} and elevated LH at higher precipitation rates, because shallow LH is essentially absent there. Therefore in general, these estimates differ from each other mainly in where their heating peaks are and whether they have just a single peak or double peaks. The differences in the oceanic low-level heating among the TRMM products are, however, in the amount and structure of the shallow LH, which is most abundant in SLH, small in CSH and TRAIN, and essentially absent in PRH. On the other hand, while all the re-analyses have low-level heating peak near the surface, the magnitude and height vary.

4.3.3 Temporal variability

The temporal characteristics of daily heating profiles can be described in terms of their primary modes of variability. Such primary modes can be extracted using various forms of empirical orthogonal function (EOF) analysis (Zhang and Hagos 2009; Hagos *et al.* 2010; Hagos 2010). Two leading rotated EOF modes, one deep, one shallow, emerge from heating profiles based on sounding observations, TRMM retrievals, and re-analyses (Fig. 14). The differences among the mean profiles (Figs. 14a and 14e) are larger than those among the deep modes (Figs. 14b and 14f) as well as the shallow modes (Figs. 14c and 14g). But, there

are discrepancies among them. The deep modes of CSH and PRH are outliers in their lack of heating at low levels. The PRH, CSH, and NCEP I (at 300hPa) deep heating peaks are higher than that of the sounding average (near 400hPa). For the shallow modes, PRH has a peak near 600hPa and JRA25 at 850hPa whereas those of the other estimates as well as the soundings are at 700hPa.

For the purpose of interpreting the variability characteristics of LH, a diabatic heating profile is designated as due either to radiation, if the vertically-integrated diabatic heating is negative, or latent heat release. In a tropical convective region such as the western Pacific warm pool, the vertical structure of heating is primarily determined by LH. An EOF analysis shows that almost all of the variability in total diabatic heating is due to LH. For both, the first two EOF modes explain about 95% of the variance (Hagos 2010). This is not surprising because, while the vertical structure of LH varies significantly, the profile of clear-sky cooling shows little variability.

An oblique rotated EOF (OREOF) analysis yielded the first mode resembling a stratiform heating profile with low-level cooling and the second OREOF resembles convective heating (Fig. 1 in Schumacher *et al.* 2007). Almost the entire diabatic heating data are composed of the two profiles. This is not by accident. If indeed mesoscale LH is primarily composed of stratiform and convective heating, they naturally should constitute the large-scale diabatic heating as well. Hagos (2010) demonstrated that the bimodal variability and the structure of the leading EOF modes alone can represent the mean diabatic heating in different climate regimes of the Tropics (Fig. 15). For all the sounding-based heating time series, the two modes account for almost all their means. It follows that the total heating is primarily composed of these two building blocks.

Comparisons of diabatic/latent heating derived from in-situ soundings, satellite observations and global re-analyses have revealed that, in general, they agree with each other on their bi-modal variability. The common bi-modal behavior comes from the composition of large-scale heating by convective and stratiform clouds. This is implicitly built into TRMM LH algorithms that depend on PR reflectivity; hence, the bi-modal variability in those products is

not surprising. The commonalities among the various products, however, appear to end at the bi-modal variability. The structures of the two leading modes, the mean profiles and the seasonal cycle vary significantly among the products. The large uncertainties defined by their disagreement inevitably affect their applications. The limited availability of sounding-based heating profiles and the large spatial variability in the vertical structure of diabatic and latent heating preclude any assumption on the realism of diabatic and latent heating profiles from TRMM and re-analyses in a region without any observations. Evaluation of diabatic and latent heating profiles from TRMM and re-analyses must be done in the context of their related large-scale circulation.

4.3.4 Vertical diabatic heating structure of the MJO

The essential roles of various diabatic heating components for the MJO have been suggested based on general circulation model (GCM) studies, including shallow convective heating (e.g., Zhang and Mu 2005; Benedict and Randall 2009; Li *et al.* 2009; Zhang and Song 2009), stratiform heating (e.g., Fu and Wang 2009; Seo and Wang 2010), and radiative heating (e.g., Lee *et al.* 2001; Raymond 2001; Sobel and Gildor 2003). A transition in the vertical heating structure during MJO evolution, namely, from shallow, to deep, and then to stratiform, has been reported based on TOGA COARE observations (Lin *et al.* 2004; Kiladis *et al.* 2005). However, this vertical tilting structure in the MJO heating field was not clearly evident in sounding observations during MISO (Katsumata *et al.* 2009), as well as in a composite study over both the Indian and western Pacific Oceans (Morita *et al.* 2006) and in a case study over the Indian Ocean during 1998/1999 winter (Jiang *et al.* 2009) based on earlier versions of TRMM heating estimates. Since diabatic heating lies at the heart of the main MJO theories as discussed in section 4.2, a comprehensive characterization of the vertical heating structure of the MJO would be of considerable value in elucidating its essential physics.

By employing diabatic heating datasets from three TRMM-based estimates (TRAIN, SLH, CSH) and three recent re-analyses (ERA-I, MERRA, CFS-R), Jiang *et al.* (2011) conducted a composite analysis of vertical anomalous heating structures associated with the MJO based on strong MJO events during boreal winter (November-April) from 1998-2007/08. The strong MJO events were selected and their phases (ranging from 1 to 8) were determined by

employing the WH index. Figure 16 illustrates vertical-temporal anomalous MJO heating profiles (shaded) based on six datasets over the western Pacific (WP, 150-160°E) and eastern equatorial Indian Ocean (EEIO, 80-90°E). All of the heating fields in Fig. 16 are averaged over latitude belts between 10°S-10°N. The time (MJO phases) in the x-axis of each panel runs from right to left so that these plots also mimic longitude-height cross-sections for an eastward moving system. The black curve in each panel denotes the evolution of TRMM 3B42 rainfall anomalies (scales on right). The results suggest that, over the WP, the heating profiles based on three re-analyses exhibit a similar vertical tilting structure (Figs. 16a-16c), although the ERA-Interim exhibits a stronger heating signal in the upper troposphere. The low-level heating below 800hPa appears around phase 3 and peaks at phase 4 prior to the maximum MJO convection in phase 5. Meanwhile, a maximum heating near 450hPa after phase 5 is discerned in all three reanalysis datasets. In addition to the upper-level heating maximum, a second peak around 600hPa is also apparent in MERRA (Fig. 16b). In contrast, the vertical tilt in the heating profiles varies among the three TRMM products. While the tilt is evident in CSH, the heating does not extend as high into the upper troposphere as in the other datasets (Fig. 16f). Although the emergence of shallow heating prior to maximum convection is also discerned in the SLH heating (Q_I - Q_R) profiles, it has much weaker amplitude below 600hPa (Fig. 16e). Meanwhile, a rather weak tilt is seen in the TRAIN profiles (Fig. 16d); instead of a slight lag in maximum convection evident in other datasets, the upper-level heating maximum is largely in phase with convection in TRAIN.

Over the EEIO, the transition from a shallow to deep heating structure during MJO evolution is again evident based on the three reanalysis datasets (Fig. 16g-16i). However, some differences in the upper-level heating profiles are noticed between the EEIO and WP. While the heating maxima around 400hPa lags the rainfall peaks over the WP, they appear with the peaks in MJO convection over the EEIO (c.f., Figs. 16a-c and 16g-i). The vertical transition from shallow to deep heating structures as seen in the reanalyses is not readily apparent in three of the TRMM-based datasets over this region (Figs. 16j-l).

Differences in vertical heating structures of the MJO between TRMM estimates and re-analyses are also noted in a similar composite study by Ling and Zhang (2011). By

illustrating vertical-temporal MJO heating structures at three longitudes (90°E, 120°E, and 150°E), but averaged over 15°S-15°N instead of 10°S-10°N as in Fig. 16, significant differences in composite vertical MJO heating structures were noted among several re-analysis datasets in addition to differences between re-analyses and TRMM estimates as mentioned above.

4.4 *Improving monsoon forecasts and model physics using the multi-model super-ensemble approach*

The vertical distribution of heating predicted by a suite of global models (Krishnamurti *et al.* 2007) was improved using a multi-model super-ensemble technique (Krishnamurti *et al.* 2000 a, b). The same approach but with a suite of mesoscale models in place of global models is being used to construct forecasts of Q_1 . The Advanced Research WRF (Weather Research and Forecasting model, ARW) V3.1.1 was used for this study. Figure 17 shows the WRF single domain configuration with 25-km horizontal resolution and 134x141x28 grid points. The PBL and surface layer parameterization employed the YSU scheme (Hong *et al.* 2006; Hong 2007) and Mellor-Yamada-Janjic¹² (Mellor and Yamada 1992) Level-2 turbulence closure model, respectively. The land surface model is based on NOAH (Chen and J. Dudhia 2001) and consists of a 4-layer soil temperature and moisture model with canopy moisture and snow cover prediction. It provides sensible and latent heat fluxes to the boundary layer scheme. The Dudhia (Dudhia 1989) and RRTM (Mlawer *et al.* 1997) broadband two-stream (upward and downward fluxes) approaches were used for the shortwave and longwave radiative flux calculations, respectively. The model was initialized from NCEP FNL operational Global Analysis data (1° x 1° spatial grid) and from which time-varying lateral boundary conditions were provided at 12-h intervals. Table 7 lists a set of model configurations put together from the available choices of different cumulus parameterizations and microphysics packages within the WRF/ARW. After some experimentation, this choice of model physics was found to be sufficiently robust to provide a reasonable ensemble spread.

¹² The scheme was coded/modified by Dr. Janjic for the NCEP Eta model.

The multi-model super-ensemble has a training and a forecast phase. During the training phase, vertical profiles of Q_I are calculated from all model forecasts. The training phase covers the 90-day period from 1 July to 31 August 2004 and 1 July to 28 August 2005. All forecasts start and end at 00 UTC. During the training phase, a super-ensemble was constructed for the geopotential height z and temperature T . Q_I is the substantial derivative of the dry static energy ($gz + c_p T$) where g is gravity and c_p the specific heat of dry air at constant pressure. The computation of Q_I entails the calculation of the local change and the advective changes (horizontal and vertical advection) of the dry static energy. The observed counterparts of Q_I for all these forecast time intervals are from the CSH algorithm.

First, the model- and super-ensemble-based forecasts of precipitation over India were validated. Those are illustrated in Figs. 18, 19 and 20. Four examples of the typical daily skill of the precipitation forecasts are shown spanning days 1 through 6. In Fig. 18a-d, the vertical bars show skill via the root mean square (rms) errors for the six model configurations and the super-ensemble for each of the forecast days. Figure 19a-d shows the daily skill based on the area-averaged correlations of the observed and simulated rainfall. The observed rain comes from the rain gauge-based estimates of Rajeevan *et al.* (2007); this is a very dense rain gauge archive that contains nearly 2300 rain gauges over India. Of interest in Figs. 18 and 19 is the slow increase in rms errors in the forecasts from day 1 to day 6 and the slow decline of the areal correlations during this forecast period. The multi-model super-ensemble performs the best in comparison to all of the member models in the forecast suite and exhibits very little decline in the correlations from day 1 to day 6; the rms errors of the multi-model super-ensemble also do not show much of an increase with forecast time. Given these improved forecasts of precipitation, it is expected that the super-ensemble would carry improved skill in terms of forecast vertical heating profiles. The model- and multi-model super-ensemble-based vertical distributions are compared with those from the CSH estimates.

Figure 20a-d illustrates the vertical profiles of area-averaged Q_I (K/day) over the Indian sub-domain ($70^\circ\text{E} - 90.17^\circ\text{E}$, $6.85^\circ\text{N} - 25.13^\circ\text{N}$). These represent four-selected map times during a four-day forecast phase of the multi-model super-ensemble. The mesoscale models have

higher values for Q_1 than the CSH values. There are many vertical details in the model-based profiles. The satellite-based CSH profiles are smooth and look parabolic along the vertical, as was also noted in Krishnamurti *et al.* (2008). The multi-model super-ensemble recognizes these differences between the CSH and the member model vertical profiles and removes the large differences that are collective systematic errors. As a result the forecasts through day 4 from the multi-model super-ensemble come out very close to the CSH profiles. The straight ensemble mean would reside between the forecast profiles of the member models and would contain large errors. In conclusion it is safe to state that given observed measures of heating such as the CSH profiles, it is possible to produce accurate forecasts of Q_1 from the construction of a multi-model super-ensemble.

5. Future Work

This paper presented some of the recent improvements in TRMM LH algorithms and their relationship with the pioneering works of Yanai *et al.* (1973). Preliminary results from an inter-comparison of the LH algorithms were also presented. Differences in the derived heating profiles from the different algorithms, including their associated level of maximum heating, could be due to the physical assumptions as well as the different LUTs (i.e., CRM-simulated heating profiles used to generate the LUTs). This inter-comparison will be continued in collaboration with those working on observed heating estimates, which could help to identify the salient physical processes leading to the similarities and differences produced by the retrieval algorithms. In addition, data from GPM field campaigns and ground validation sites (e.g., MC3E) that provide extensive and high quality in situ microphysical observations will be valuable in improving and validating CRM microphysics. This is important because representative microphysics is essential in reproducing, within a modeling framework, the key 4D features of LH.

This paper also presented highlights published in the *J. of Climate* special collection on TRMM diabatic heating. In particular, the comparison of heating profiles derived from TRMM LH algorithms, sounding networks and reanalyses over the Tropics were discussed. One key finding was that the major differences between the heating structures from the

various estimates are related to low-level heating and the level of maximum heating. Low-level heating is also important for the MJO cycle. Given the uncertainties in TRMM-based diabatic heating estimates, the central role of diabatic heating for the MJO, and the demands for reducing model deficiencies in simulating the MJO, there is a great interest and urgent need to examine the MJO vertical heating structure and related processes in current GCMs and to explore how their structure and fidelity relate to the models' MJO representation and forecast skill. To help address these objectives, a model and observation inter-comparison project on vertical heating structures and diabatic processes associated with the MJO is being organized through a joint effort by the WCRP (World Climate Research Program) – WWRP (World Weather Research Program) YOTC (Year of Tropical Convection) MJO Task Force and GEWEX Atmospheric System Study Project (Petch *et al.* 2011; www.ucar.edu/yotc/mjodiab.html).

5.1 *Standard LH products*

The PMM joint science team has decided to have two standard LH algorithms: the Goddard CSH algorithm and the SLH algorithm. Table 8 lists the required data and type of heating products for these two algorithms. Note that one of the major inputs for these standard products is the improved rainfall estimate. Figure 21 shows an example of the LH products generated from the new version of the CSH algorithm.

Standard LH products from TRMM will represent a valuable new source of data for the research community, products that, a decade ago, were considered beyond reach. These data products will enable compelling new investigations into the complexities of storm life cycles, diabatic heating controls and feedbacks related to meso/synoptic circulations and the influence of diabatic heating on the Earth's general circulation and climate. In particular, the LH estimates will be of great help as a benchmark for a model inter-comparison study on vertical MJO heating structures as shown in section 4.3 and for the model intercomparison experiment mentioned above. The standard LH products could help to determine how well the model-simulated heating structures agree with observations and determine how different

they are relative to the spread of observational (reanalysis and TRMM) values, which would also address the question of how useful the observations are at this point.

5.2 *Future directions*

Since temperature (heating) and water vapor (moistening/drying) are closely related (Yanai *et al.* 1973), it is proposed to produce both heating and moistening profiles using GPM rainfall products. Both LH and moistening profiles are also needed for improving large-scale model simulations and forecasts (Rajendran *et al.* 2002). GPM will produce higher temporal (three-hourly) and spatial resolution (up to 0.05 degree) rainfall products. Several issues need therefore to be addressed. CRM results have shown that the horizontal eddy term is quite small if averaged over a large area. In addition, the CRM results have indicated that the horizontal and vertical eddy transport terms usually counteract each other (mass continuity) over small spatial scales (cloud scales). The contribution by horizontal and vertical eddy heat and moisture transport to the heat and moisture budgets must be examined at various horizontal resolutions (e.g., TRMM and GPM satellite footprint sizes). It may be necessary to produce heating and moistening profiles including all of the eddy transport and microphysics terms.

Only a limited number of CRM-simulated cases were used to build the SLH and CSH algorithm (see section 2) LUTs. Observations from additional field experiments (e.g., TWP-ICE, MC³E, DYNAMO) and future GV site(s) will be needed to provide new types of initial conditions to CRMs to expand the number of cases and environments represented in the LUTs. In addition, large-scale reanalysis products such as MERRA can be used both to improve cloud-resolving simulations by placing them in a larger-scale dynamical context and to expand the range of environmental conditions explored by CRM simulations beyond field experiments. Figure 22 depicts preliminary results comparing simulations forced by the SCSMEX sounding network versus simulations forced by MERRA on GCE grid boundaries in the same location. The simulations forced by MERRA produce rainfall and precipitable water at least as close to the observed as the sounding-forced simulations with some improvement in precipitable water relative to the sounding forcing. This suggests that the GCE-MERRA approach has the potential to provide reasonably good quality simulations to

the heating algorithms for a variety of locations and conditions, including those regions with large surface rainfall, such as the Indian Ocean, SPCZ, S. America, Africa, and snow events, which are not well represented in the current LUTs. In addition to expanding the number and type of environments, further improvements to the CSH LUTs will be made by using the improved and validated physics in the GCE and running cases at higher resolution. The GCE+MERRA simulated cloud datasets in the Cloud Data Library (<http://cloud.gsfc.nasa.gov>) can be used to improve the performance of satellite-based rainfall and LH retrievals through more representative LUTs and to improve moist process parameterizations for GCMs.

6. Acknowledgements

The authors extend their heartfelt appreciation to Professor Michio Yanai of the University of California at Los Angeles. The enthusiasm of Dr. Yanai over the years and his willingness to discuss ideas concerning the subject of atmospheric latent heating and its implications with the various authors has had a profound influence on ideas central to this paper. We also appreciate the leadership of Dr. Joanne Simpson, a close colleague of Dr. Yanai and the first TRMM project scientist, who promoted LH as being one of the two key products for TRMM.

Acknowledgment is also made to the NASA Center for Climate Simulation (NCCS) at NASA Goddard Space Flight Center for computer time used in this research. Finally, the authors appreciate the implementation of LH retrieval algorithms into the Precipitation Processing System also at the NASA Goddard Space Flight Center for the production of standardized LH products. This research has been supported by an assortment of PMM Science Team grants under the auspices of both the National Aeronautics and Space Administration (NASA) and the Japan Aerospace Exploration Agency (JAXA). D. Waliser's contribution was carried out on behalf of the Jet Propulsion Laboratory, California Institute of Technology, under a contract with NASA.

References

- Benedict, J. J., and D. A. Randall, 2009: Structure of the Madden-Julian Oscillation in the Superparameterized CAM. *J. Atmos. Sci.*, **66**, 3277-3296.
- Bretherton, C., M. E. Peters, and L. E. Back, 2004: Relationships between Water Vapor Path and Precipitation over the Tropical Oceans, *J. Climate*, **17**, 1517-1528.
- Chang, C.-P. and H. Lim, 1988: Kelvin Wave-CISK: A Possible Mechanism for the 30-50 Day Oscillations. *J. Atmos. Sci.*, **45**, 1709-1720.
- Chen, F., and J. Dudhia, 2001: Coupling an advanced land-surface/ hydrology model with the Penn State/ NCAR MM5 modeling system. Part I: Model description and implementation. *Mon. Wea. Rev.*, **129**, 569–585.
- Chikira, M., and M. Sugiyama, 2010: A cumulus parameterization with state-dependent entrainment rate. Part I: Description and sensitivity to temperature and humidity profiles. *J. Atmos. Sci.*, **67**, 2171-2193.
- Ciesielski, P. E., and R. H. Johnson, 2006: Contrasting characteristics of convection over the northern and southern South China Sea during SCSMEX. *Mon. Wea. Rev.*, **134**, 1041-1062.
- Del Genio, A. D., Y.-H. Chen, D.-H. Kim, and M.-S. Yao, 2012: The MJO transition from shallow to deep convection in Cloudsat/CALIPSO data and GISS GCM simulations. *J. Climate*, **25**, 3755-3770.
- Dudhia, J., 1989: Numerical study of convection observed during the winter monsoon experiment using a mesoscale two-dimensional model, *J. Atmos. Sci.*, **46**, 3077–3107.
- Fairall, C., E. F. Bradley, D. P. Rogers, J. B. Edson, and G. S. Young, 1996: Bulk parameterization of air-sea fluxes for TOGA COARE. *J. Geophys. Res.*, **101**, 3747–3764.
- Fu, X. H., and B. Wang, 2009: Critical Roles of the Stratiform Rainfall in Sustaining the Madden-Julian Oscillation: GCM Experiments. *J. Clim.*, **22**, Doi 10.1175/2009jcli2610.1, 3939-3959.
- Gamache, J. F., and R. A. Houze Jr., 1983: Water budget of a mesoscale convective system in the Tropics. *J. Atmos. Sci.*, **40**, 1835–1850.
- Ciesielski, P. E., R. H. Johnson, P. T. Haertel, and J. Wang, 2003: Corrected TOGA COARE sounding humidity data: Impact on diagnosed properties of convection and climate over the warm pool. *J. Climate*, **16**, 2370-2384.

- Gottschalck, J., M. Wheeler, K. Weickmann, F. Vitart, N. Savage, H. Lin, H. Hendon, D. Waliser, K. Sperber, M. Nakagawa, C. Prestrelo, M. Flatau, and W. Higgins, 2010: A Framework for Assessing Operational Madden–Julian Oscillation Forecasts: A CLIVAR MJO Working Group Project. *Bull. Am. Meteorol. Soc.*, **91**, doi:10.1175/2010BAMS2816.1, 1247–1258.
- Grell, G. A., and D. Devenyi, 2002: A generalized approach to parameterizing convection combining ensemble and data assimilation techniques. *Geophys. Res. Lett.*, **29**(14), Article 1693.
- Grecu, M., and W. S. Olson, 2006: Bayesian estimation of precipitation from satellite passive microwave observations using combined radar-radiometer retrievals. *Applied Meteor. Climatol.*, **45**, 416–433.
- Grecu, M., W. Olson, C.-L. Shie, T. L’Ecuyer, and W.-K. Tao, 2009: Combining Satellite Microwave Radiometer and Radar Observations to Estimate Atmospheric Latent Heating Profiles. *J. Climate*, **22**, 6356–6376.
- Hagos S., and C. Zhang C. 2009. Diabatic heating, divergent circulation and moisture transport in the African monsoon system. *Q. J. R. Meteorol. Soc.* **136**(S1): 411–425.
- Hagos, S., and Coauthors, 2010: Estimates of tropical diabatic heating profiles: Commonalities and uncertainties. *J. Climate*, **23**, 542–558.
- Hendon, H. H., and M. L. Salby, 1994: The Life Cycle of the Madden-Julian Oscillation. *J. Atmos. Sci.*, **51**, 2225–2237.
- Hirota, N., Y. N. Takayabu, M. Watanabe, and M. Kimoto, 2011: Precipitation reproducibility over tropical oceans and its relationship to the double ITCZ problem in CMIP3 and MIROC5 climate models. *J. Climate*, **24**, 4859–4873.
- Hong, S.-Y., J. Dudhia, and S.-H. Chen, 2004: A Revised Approach to Ice Microphysical Processes for the Bulk Parameterization of Clouds and Precipitation, *Mon. Wea. Rev.*, **132**, 103–120.
- Hong, S.-Y., and J.-O. J. Lim, 2006: The WRF Single-Moment 6-Class Microphysics Scheme (WSM6), *J. Korean Meteor. Soc.*, **42**, 129–151.
- Hong, S.-Y., and Y. Noh, and J. Dudhia, 2006: A new vertical diffusion package with an explicit treatment of entrainment processes. *Mon. Wea. Rev.*, **134**, 2318–2341.

- Hong, S.-Y., 2007: Stable Boundary Layer Mixing in a Vertical Diffusion Scheme. *The Korea Meteor. Soc.*, Fall conference, Seoul, Korea, Oct. 25-26.
- Houze, R. A., Jr., 1997: Stratiform precipitation in regions of convection: A meteorological paradox. *Bull. Amer. Meteor. Soc.*, **78**, 2179-2196.
- Houze, R. A., Jr., 1982: Cloud clusters and large-scale vertical motions in the tropics. *J. Meteor. Soc. Japan*, **60**, 396-409.
- Jakob, C., and C. Schumacher, 2008: Precipitation and latent heating characteristics of the major tropical Western Pacific cloud regimes. *J. Climate*, **21**, 4348-4364.
- Janjic, Z. I., 1994: The step-mountain eta coordinate model: further developments of the convection, viscous sublayer and turbulence closure schemes, *Mon. Wea. Rev.*, **122**, 927–945.
- Janjic, Z. I., 2000: Comments on "Development and Evaluation of a Convection Scheme for Use in Climate Models", *J. Atmos. Sci.*, **57**, p. 3686.
- Jiang, X., D. E. Waliser, M. C. Wheeler, C. Jones, M. N. Lee, and S. D. Schuert, 2008: Assessing the skill of an all-season statistical forecast model for the Madden-Julian oscillation. *Mon. Weather Rev.*, **136**, DOI:10.1175/2007MWR2305.1, 1940-1956.
- Jiang, X., D. E. Waliser, W. S. Olson, W.-K. Tao, T. S. L'Ecuyer, J.-L. Li, B. Tian, Y. L. Yung, A. M. Tompkins, S. E. Lang, and M. Grecu, 2009: Vertical Heating Structures Associated with the MJO as Characterized by TRMM Estimates, ECMWF Reanalyses, and Forecasts: A Case Study during 1998/99 Winter. *J. Clim.*, **22**, doi:10.1175/2009JCLI3048.1, 6001-6020.
- Jiang, X., D. E. Waliser, W. S. Olson, W.-K. Tao, T. S. L'Ecuyer, K.-F. Li, Y. L. Yung, S. Shige, S. Lang, and Y. N. Takayabu, 2011: Vertical Diabatic Heating Structure of the MJO: Intercomparison between Recent Reanalyses and TRMM Estimates. *Mon. Weather Rev.*, **139**, 10.1175/2011mwr3636.1, 3208-3223.
- Johnson, R. H., and P. J. Hamilton, 1988: The relationship of surface pressure features to the precipitation and airflow structure of an intense mid-latitude squall line. *Mon. Wea. Rev.*, **116**, 1444-1471.
- Johnson, R. H., 1984: Partitioning tropical heat and moisture budgets into cumulus and mesoscale components: Implication for cumulus parameterization. *Mon. Wea. Rev.*, **112**, 1656-1665.

- Johnson, R. H., and P.E. Ciesielski, 2000: Rainfall and radiative heating rates from TOGA_COARE atmospheric budgets. *J. Atmos. Sci.*, **57**, 1497-1514.
- Johnson, R. H., and P. E. Ciesielski, 2002: Characteristics of the 1998 summer monsoon onset over the northern South China Sea. *J. Meteor. Soc. Japan*, **80**, 561–578.,
- Kain J. S., and M. Fritsch 2004: The Kain-Fritsch convective parameterization: An update. *J. Appl. Meteor.*, **43**, 170–181.
- Kalnay, E., and Coauthors, 1996: The NCEP/NCAR 40-Year Reanalysis Project. *Bull. Amer. Meteor. Soc.*, **77**, 437–471.
- Kanamitsu, M., W. Ebisuzaki, J. Woolen, S. K. Yang, J. J. Hnilo, M. Fiorino, and G. L. Potter, 2002: NCEP–DOE AMIP-II Reanalysis (R-2). *Bull. Amer. Meteor. Soc.*, **83**, 1631-1643.
- Katsumata, M., R. H. Johnson, and P. E. Ciesielski, 2009: Observed synoptic-scale variability during the developing phase of an ISO over the Indian Ocean during MISO. *J. Atmos. Sci.*, **66**, 3434-3448
- Kessler, E., 1969: On the distribution and continuity of water substance in atmospheric circulation, *Meteor. Monogr.*, **32**, Amer. Meteor. Soc., 84 pp.
- Kiladis, G. N., K. H. Straub, and P. T. Haertel, 2005: Zonal and Vertical Structure of the Madden-Julian Oscillation. *J. Atmos. Sci.*, **62**, 2790-2809.
- Kim, D., et al., 2009: Application of MJO Simulation Diagnostics to Climate Models. *J. Clim.*, **22**, Doi 10.1175/2009jcli3063.1, 6413-6436.
- Krishnamurti T.N., C. Gnanaseelan, and A. Chakraborty, 2007: Prediction of the diurnal cycle using a multimodel superensemble. Part1: Precipitation. *Mon. Wea. Rev.*, **135**, 3613-3632.
- Krishnamurti T.N., C.M. Kishitawal, Z. Zhang, T. Larow, D. Bachiochi, E. Williford, 2000: Multimodel ensemble forecasts for weather and seasonal climate. *J Climate*, **13**, 4196–4216.
- Krishnamurti T. N., C. M. Kishtawal, W. D. Shin, and C. E. Williford, 2000: Improving tropical precipitation forecasts from a Multianalysis Superensemble, *J. Climate*, **13**, 4217–4227.
- Krueger, S.K., 1988: Numerical simulation of tropical cumulus clouds and their interaction with the subcloud layer. *J. Atmos. Sci.*, **45**, 2221-2250.
- Kummerow, C., W. Barnes, T. Kozu, J. Shiue, and J. Simpson, 1998: The Tropical Rainfall Measurement Mission (TRMM) sensor package. *J. Atmos. Ocn. Tech.*, **15**, 809-817.

- Lang, S., W.-K. Tao, R. Cifelli, W. Olson, J. Halverson, S. Rutledge, and J. Simpson, 2007: Improving simulations of convective system from TRMM LBA: Easterly and Westerly regimes. *J. Atmos. Sci.*, **64**, 1141-1164.
- Lang, S., W.-K. Tao, and X. Zeng, 2011: Reducing the biases in simulated radar reflectivities from a bulk microphysics scheme: Tropical convective systems, *J. Atmos. Sci.*, **68**, 2306-2320.
- Lau, W. K.-M., and L. Peng, 1987: Origin of Low-Frequency (Intraseasonal) Oscillations in the Tropical Atmosphere. Part I: Basic Theory. *J. Atmos. Sci.*, **44**, 950-972.
- Lau, W. K.-M., and Coauthors, 2000: A report of the field operations and early results of the South China Sea Monsoon Experiment (SCSMEX). *Bull. Amer. Meteor. Soc.*, **81**, 1261-1270.
- Lau, W. K.-M., H-T. Wu, 2010: Characteristics of Precipitation, Cloud, and Latent Heating Associated with the Madden–Julian Oscillation. *J. Climate*, **23**, 504–518.
- Lau, W. K.-M., and D. E. Waliser, 2011: *Intraseasonal Variability in the Atmosphere-Ocean Climate System*. Second ed. Springer, 613p, Heidelberg, Germany.
- Lee, M. I., I. S. Kang, J. K. Kim, and B. E. Mapes, 2001: Influence of cloud-radiation interaction on simulating tropical intraseasonal oscillation with an atmospheric general circulation model. *J. Geophys. Res.*, **106**, 14219-14233.
- Li, C. Y., X. L. Jia, J. Ling, W. Zhou, and C. D. Zhang, 2009: Sensitivity of MJO simulations to diabatic heating profiles. *Climate Dyn.*, **32**, Doi 10.1007/S00382-008-0455-X, 167-187.
- Lin, J.-L., et al., 2006: Tropical Intraseasonal Variability in 14 IPCC AR4 Climate Models. Part I: Convective Signals. *J. Clim.*, **19**, 2665-2690.
- Lin, J., B. Mapes, M. Zhang, and M. Newman, 2004: Stratiform Precipitation, Vertical Heating Profiles, and the Madden-Julian Oscillation. *J. Atmos. Sci.*, **61**, 296-309.
- Lin, J. L., and B. E. Mapes, 2004: Radiation budget of the tropical intraseasonal oscillation. *J. Atmos. Sci.*, **61**, 2050-2062.
- Li, X., C.-H. Sui, K.-M. Lau, and M.-D. Chou, 1999: Large-scale forcing and cloud–radiation interaction in the tropical deep convective regime. *J. Atmos. Sci.*, **56**, 3028–3042
- Lin, X., and R.H. Johnson, 1996: Heating, moistening and rainfall over the western Pacific during TOGA COARE. *J. Atmos. Sci.*, **53**, 3367-3383.

- Ling, J., and C. D. Zhang, 2011: Structural Evolution in Heating Profiles of the MJO in Global Reanalyses and TRMM Retrievals. *J. Clim.*, **24**, 10.1175/2010jcli3826.1, 825-842.
- Ling, J., and C. D. Zhang, 2012: Diabatic heating profiles in recent global reanalyses. *J. Clim.*, (submitted).
- L'Ecuyer, T. S., and G. L. Stephens, 2003: The tropical oceanic energy budget from the TRMM perspective. Part I: Algorithm and uncertainties. *J. Climate*, **16**, 1967-1985.
- L'Ecuyer, T. S., and G. L. Stephens, 2007: The tropical atmospheric energy budget from the TRMM perspective. Part II: Evaluating GCM representations of the sensitivity of regional energy and water cycles to the 1998-1999 ENSO cycle. *J. Climate*, **20**, 4548-4571.
- Madden, R. A., and P. R. Julian, 1971: Detection of a 40-50 Day Oscillation in Zonal Wind in Tropical Pacific. *J. Atmos. Sci.*, **28**, 702-&.
- Madden, R. A., and P. R. Julian, 1994: Observations of the 40-50-Day Tropical Oscillation: A Review. *Mon. Weather Rev.*, **122**, 814-837.
- Maloney, E. D., and D. L. Hartmann, 1998: Frictional Moisture Convergence in a Composite Life Cycle of the Madden-Julian Oscillation. *J. Clim.*, **11**, 2387-2403.
- Mapes, B. E., 2000: Convective Inhibition, Subgrid-Scale Triggering Energy, and Stratiform Instability in a Toy Tropical Wave Model. *J. Atmos. Sci.*, **57**, 1515-1535.
- Masunaga, H., T. S. L'Ecuyer, and C. D. Kummerow, 2005: Variability in the characteristics of precipitation systems in the tropical Pacific. Part I: Spatial structure. *J. Climate*, **18**, 823-840.
- Matsui, T., X. Zeng, W.-K. Tao, H. Masunaga, W. S. Olson, and S. Lang, 2009: Evaluation of long-term cloud-resolving model simulations using satellite radiance observations and multi-frequency satellite simulators. *J. Atmos. Oce. Tech.* **26**, 1261-1274.
- May, P. T., J. H. Mather, G. Vaughan, C. Jakob, G. M. McFarquar, K. N. Bower, and G. G. Mace, 2008: The Tropical Warm Pool International Cloud Experiment (TWP-ICE), *Bull. Amer. Meteor. Soc.*, in press.
- Mestas-Nuñez, A.M., 2000: Orthogonality properties of rotated empirical modes. *I. J. Climatol.*, **20**, 1509-1516.

- Mlawer, E. J., S. J. Taubman, P. D. Brown, M. J. Iacono, and S. A. Clough, 1997: Radiative transfer for inhomogeneous atmosphere: RRTM, a validated correlated-k model for the longwave. *J. Geophys. Res.*, **102** (D14), 16663–16682.
- Moncrieff, M. W., S. K. Krueger, D. Gregory, J.-L. Redelsperger, and W.-K. Tao, 1997: GEWEX Cloud System Study (GCSS) Working Group 4: Precipitating convective cloud systems, *Bull. Amer. Meteor. Soc.*, **78**, 831-845.
- North, G. R., T. L. Bell, R. F. Cahalan, and F. J. Moeng, 1982: Sampling Errors in the Estimation of Empirical Orthogonal Functions. *Mon. Wea. Rev.*, **110**, 699–706.
- Olson, W. S., C. D. Kummerow, Y. Hong, and W.-K. Tao, 1999: Atmospheric latent heating distributions in the tropics derived from passive microwave radiometer measurements. *J. Appl. Meteor.*, **38**, 633-664.
- Olson, W. S., C. D. Kummerow, S. Yang, G. W. Petty, W.-K. Tao, T. L. Bell, S. A. Braun, Y. Wang, S. E. Lang, D. E. Johnson, and C. Chiu, 2006: Precipitation and latent heating distributions from satellite passive microwave radiometry. Part I: Method and uncertainties. *J. Appl. Meteor.*, **45**, 702–720.
- Onogi, K., and Coauthors, 2007: The JRA-25 Reanalysis. *J. Meteor. Soc. Japan*, **85**, 369-432.
- Petch, J., D. Waliser, X. Jiang, P. Xavier, and S. Woolnough, 2011: A global model inter-comparison of the physical processes associated with the MJO, *GEWEX News*, Vol. 21, No. 3, Pages 3-5.
- Raymond, D. J., 2001: A new model of the Madden-Julian oscillation. *J. Atmos. Sci.*, **58**, 2807-2819.
- Raymond, D. J., and H. Jiang, 1990: A Theory for Long-Lived Mesoscale Convective Systems. *J. Atmos. Sci.*, **47**, 3067–3077.
- Randall, D., S. Krueger, C. Bretherton, J. Curry, P. Duynkerke, M. Moncrieff, B. Ryan, D. Starr, M. Miller, W. Rossow, G. Tselioudis, and B. Wielicki, 2003: Confronting models with data: The GEWEX Cloud Systems Study. *Bull. Amer. Meteor. Soc.*, **84**, 455–469.
- Rodgers, E. B., W. S. Olson, V. M. Karyampudi, and H. F. Pierce, 1998: Satellite-derived latent heating distribution and environmental influences in Hurricane Opal (1995). *Mon. Wea. Rev.*, **126**, 1229-1247.

- Rodgers, E. B., W. Olson, J. Halverson, J. Simpson, and H. Pierce, 2000: Environmental forcing of supertyphoon Paka's (1997) latent heat structure. *J. Appl. Meteor.*, **39**, 1983-2006.
- Rutledge, S. A., and R. A. Houze, Jr., 1987: A diagnostic modeling study of the trailing stratiform rain of a mid latitude squall line. *J. Atmos. Sci.*, **44**, 2640-2656.
- Satoh, S., and A. Noda, 2001: Retrieval of latent heating profiles from TRMM radar data. *Proceedings of 30th International Conf. on Radar Meteorology*, [Munich, Germany; 19-24 July 2001], 340-342.
- Schumacher, C., M. H. Zhang, and P. E. Ciesielski, 2007: Heating Structures of the TRMM Field Campaigns. *J. Atmos. Sci.*, **64**, 2593-2610.
- Seo, K. H., and W. Q. Wang, 2010: The Madden-Julian Oscillation Simulated in the NCEP Climate Forecast System Model: The Importance of Stratiform Heating. *J. Clim.*, **23**, Doi 10.1175/2010jcli2983.1, 4770-4793.
- Sherwood, S. C., 1999: Convective precursors and predictability in the tropical western Pacific. *Mon. Wea. Rev.*, **127**, 2977-2991.
- Shige, S., Y. N. Takayabu, W.-K. Tao, and D. E. Johnson: 2004, Spectral retrieval of latent heating profiles from TRMM PR data. Part I: Development of a model-based algorithm. *J. Appl. Meteor.*, **43**, 1095-1113.
- Shige, S., Y. N. Takayabu, W.-K. Tao, and C.-L. Shie, 2007: Spectral retrieval of latent heating profiles from TRMM PR data. Part II: Algorithm improvement and heating estimates over tropical ocean regions. *J. Appl. Meteor. Climatol.*, **46**, 1098-1124.
- Shige, S., Y. N. Takayabu, and W.-K. Tao, 2008: Spectral retrieved of latent heating profiles from TRMM PR data. Part III: Moistening estimates over the tropical ocean regions *J. Applied Meteor. Climatology*, **47**, 620--640.
- Shige, S., Y. N. Takayabu, S. Kida, W.-K. Tao, X. Zeng and T. L'Ecuyer, 2009: Spectral retrieved of latent heating profiles from TRMM PR data. Part VI: Comparisons of lookup tables from two- and three-dimensional simulations. *J. Climate*, **22**, 5577-5594.
- Short D. A., and K. Nakamura, 2000: TRMM radar observations of shallow precipitation over the tropical oceans. *J. Climate*, **13**, 4107-4124.
- Silva Dias, 2002: Cloud and rain processes in a biosphere-atmosphere interaction context in the Amazon Region. *J. Geophys. Res.*, **107**(d20): 8072.

- Slingo, J. M., P. M. Inness, and K. R. Sperber, 2005: Modeling. *Intraseasonal Variability in the Atmosphere-Ocean Climate System*, W. K. M. Lau and D. E. Waliser, Eds., Springer, Heidelberg, Germany, 361-388.
- Sobel, A. H., and H. Gildor, 2003: A simple time-dependent model of SST hot spots. *J. Clim.*, **16**, 3978-3992.
- Soong, S.-T., and W.-K. Tao, 1980: Response of deep tropical clouds to mesoscale processes. *J. Atmos. Sci.*, **37**, 2016-2036.
- Stephens, G. L., P. J. Webster, R. H. Johnson, R. Engelen, and T. L'Ecuyer, 2004: Observational evidence for the mutual regulation of the tropical hydrological cycle and tropical sea surface temperatures. *J. Clim.*, **17**, 2213-2224.
- Sui, C-H., and M. Yanai, 1986: Cumulus ensemble effects on the large-scale vorticity and momentum fields of GATE. Part I: Observational evidence. *J. Atmos. Sci.*, **43**, 1618-1642.
- Takemi, T., O. Hirayama, and C. Liu, 2004: Factors responsible for the vertical development of tropical oceanic cumulus convection. *Geophys. Res. Lett.*, **31**, L11109, doi:10.1029/2004GL020225.
- Takayabu, Y.N., 2002: Spectral representation of rain features and diurnal variations observed with TRMM PR over the equatorial areas. *Geophys. Res. Lett.*, **29**, 301-304.
- Takayabu, Y. N., J. Yokomori, and K. Yoneyama, 2006: A diagnostic study on interactions between atmospheric thermodynamic structure and cumulus convection over the tropical western Pacific Ocean and over the Indochina Peninsula. *J. Meteor. Soc. Japan*, **84A**, 151-169.
- Takayabu, Y. N., S. Shige, W.-K. Tao, and N. Hirota, 2010: Shallow and deep latent heating modes over tropical oceans observed with TRMM PR Spectral Latent Heating data, *J. Climate*, **23**, 2030-2046.
- Tao, W.-K., and S.-T. Soong, 1986: A study of the response of deep tropical clouds to mesoscale processes: Three-dimensional numerical experiments. *J. Atmos. Sci.*, **43**, 2653-2676.
- Tao, W.-K., J. Simpson, and S.-T. Soong, 1987: Statistical properties of a cloud ensemble: A numerical study. *J. Atmos. Sci.*, **44**, 3175-3187.
- Tao, W.-K., and J. Simpson, 1989: Modeling study of a tropical squall-type convective line. *J. Atmos. Sci.*, **46**, 177-202.

- Tao, W.-K., J. Simpson, S. Lang, M. McCumber, R. Adler, and R. Penc, 1990: An algorithm to estimate the heating budget from vertical hydrometeor profiles. *J. Appl. Meteor.*, **29**, 1232-1244.
- Tao, W.-K., and J. Simpson, 1993: The Goddard Cumulus Ensemble Model. Part I: Model description. *Terr. Atmos. Oceanic Sci.*, **4**, 19–54.
- Tao, W.-K., S. Lang, J. Simpson, and R. Adler, 1993: Retrieval algorithms for estimating the vertical profiles of latent heat release: Their applications for TRMM. *J. Meteor. Soc. Japan*, **71**, 685-700.
- Tao, W. -K., S. Lang, J. Simpson, W. S. Olson, D. Johnson, B. Ferrier, C. Kummerow, and R. Adler, 2000: Retrieving vertical profiles of latent heat release in TOGA COARE convective systems using a cloud resolving model, SSM/I and radar data. *J. Meteor. Soc. Japan*, **78**, 333–355.
- Tao, W.-K., S. Lang, W.S. Olson, S. Yang, R. Meneghini, J. Simpson, C. Kummerow, E. Smith and J. Halverson, 2001: Retrieved vertical profiles of latent heating release using TRMM rainfall products for February 1998. *J. Appl. Meteor.*, **40**, 957-982.
- Tao, W.-K., 2003: Goddard Cumulus Ensemble (GCE) model: Application for understanding precipitation processes, *AMS Meteorological Monographs - Cloud Systems, Hurricanes and TRMM*, **29**, 107-138.
- Tao, W.-K., C.-L. Shie, R. Johnson, S. Braun, J. Simpson, and P.E. Ciesielski, 2003b: Convective systems over the South China Sea: Cloud resolving model simulations. *J. Atmos. Sci.*, **60**, 2929-2956.
- Tao, W.-K., D. Johnson, C.-L. Shie, and J. Simpson. 2004: Atmospheric energy budget and large-scale precipitation efficiency of convective systems during TOGA COARE, GATE, SCSMEX and ARM: Cloud-resolving model simulations, *J. Atmos. Sci.*, **61**, 2405-2423.
- Tao, W.-K., E. A. Smith, R. F. Adler, Z. S. Haddad, A. Y. Hou, T. Iguchi, R. Kakar, T. N. Krishnamurti, C. D. Kummerow, S. Lang, R. Meneghini, K. Nakamura, T. Nakazawa, K. Okamoto, W. S. Olson, S. Satoh, S. Shige, J. Simpson, Y. Takayabu, G. J. Tripoli, and S. Yang, 2006: Retrieval of latent heating from TRMM measurements. *Bull. Amer. Meteor. Soc.*, **87**, 1555-1572.
- Tao, W.-K., 2007: Cloud resolving modeling. *J. Meteor. Soc. Japan*, **85B**, 305-330.

- Tao, W.-K., and M. Moncrieff, 2009: Multi-scale cloud-system modeling. *Rev. Geophys.*, **47**, RG4002, doi:10.1029/2008RG000276.
- Tao, W.-K., S. Lang, X. Zeng, S. Shige, and Y. Takayabu, 2010: Relating convective and stratiform rain to latent heating, *J. Climate*, **23**, 1874-1893.
- Uppala, S. M., et al., 2005: The ERA-40 Re-analysis, *Q. J. R. Meteorol. Soc.*, **131**, 2961–3012.
- Webster, P. J., and R. Lukas, 1992: TOGA-COARE: The Coupled Ocean-Atmosphere Response Experiment. *Bull. Amer. Meteor. Soc.*, **73**, 1377-1416.
- Wang, B., and H. Rui, 1990: Dynamics of the Coupled Moist Kelvin-Rossby Wave on an Equatorial Beta-Plane. *J. Atmos. Sci.*, **47**, 397-413.
- Waliser, D. E., 2005: Predictability and Forecasting. *Intraseasonal Variability in the Atmosphere-Ocean Climate System*, W. K. M. Lau and D. E. Waliser, Eds., Springer, Heidelberg, Germany, 474.
- Waliser, D. E., 2006: Predictability of tropical intraseasonal variability. *Predictability of weather and climate*, T. Palmer and R. Hagedorn, Eds., Cambridge University Press 718.
- Waliser, D. E., et al., 2006: The Experimental MJO Prediction Project. *Bull. Am. Meteorol. Soc.*, **87**, 425-431.
- Wang, B., and H. Rui, 1990: Dynamics of the Coupled Moist Kelvin-Rossby Wave on an Equatorial Beta-Plane. *J. Atmos. Sci.*, **47**, 397-413.
- Wheeler, M. C., and H. H. Hendon, 2004: An All-Season Real-Time Multivariate MJO Index: Development of an Index for Monitoring and Prediction. *Mon. Weather Rev.*, **132**, 1917-1932.
- Yanai, M. 1961: Dynamical Aspects of Typhoon Formation, *J. Meteor. Soc. Japan*, **39**, 187-214.
- Yanai, M., S. Esbensen, and J. H. Chu, 1973: Determination of bulk properties of tropical cloud clusters from large-scale heat and moisture budgets. *J. Atmos. Sci.*, **30**, 611-627.
- Yang, S., and E. A. Smith, 1999a: Moisture budget analysis of TOGA-COARE area using SSM/I retrieved latent heating and large scale Q2 estimates. *J. Atmos. Oceanic Technol.*, **16**, 633-655.
- Yang, S., and E. A. Smith, 1999b: Four dimensional structure of monthly latent heating derived from SSM/I satellite measurements. *J. Clim.*, **12**, 1016-1037.

- Yang, S., and E. A. Smith, 2000: Vertical structure and transient behavior of convective-stratiform heating in TOGA-COARE from combined satellite-sounding analysis. *J. Appl. Meteor.*, **39**, 1491-1513.
- Yoneyama K., Y. Masumoto, Y. Kuroda, M. Katsumata, K. Mizuno, et al., 2008: MISMO Field Experiment in the Equatorial Indian Ocean. *Bull. Amer. Meteor. Soc.*, **89**, 1889-1903.
- Yuter, S. E., and R. A. Houze, Jr., 1995: Three-dimensional kinematic and microphysical evolution of Florida cumulonimbus. Part II: Frequency distributions of vertical velocity, reflectivity, and differential reflectivity. *Mon. Wea. Rev.*, **123**, 1941-1963.
- Yuter, S. E., R. A. Houze, Jr., E. A. Smith, T. T. Wilheit, and E. Zipser, 2005: Physical characterization of tropical oceanic convection observed in KWAJEX. *J. Appl. Meteor.*, **44**, 385-415.
- Zhang, C. D., 2005: Madden-Julian oscillation. *Rev. Geophys.*, **43**, RG2003, DOI: 10.1029/2004RG000158, 36.
- Zhang, C. D., and S. M. Hagos, 2009: Bi-modal structure and variability of large-scale diabatic heating in the tropics. *J. Atmos. Sci.*, **66**, 3621-3640.
- Zhang, C. D., J. A. Ling, S. Hagos, W. K. Tao, S. Lang, Y. N. Takayabu, S. Shige, M. Katsumata, W. S. Olson, and T. L'Ecuyer, 2010: MJO Signals in Latent Heating: Results from TRMM Retrievals. *J. Atmos. Sci.*, **67**, Doi 10.1175/2010jas3398.1, 3488-3508.
- Zhang, G. J., and M. Mu, 2005: Effects of modifications to the Zhang-McFarlane convection parameterization on the simulation of the tropical precipitation in the National Center for Atmospheric Research Community Climate Model, version 3. *J. Geophys. Res.*, **110**, 10.1029/2004jd005617, D09109.
- Zhang, G. J., and X. L. Song, 2009: Interaction of deep and shallow convection is key to Madden-Julian Oscillation simulation. *Geophys. Res. Lett.*, **36**, Doi 10.1029/2009gl037340.
- Zhang, M-H., and J. L. Lin, 1997: Constrained variational analysis of sounding data based on column-integrated budgets of mass, moisture, and momentum: Approach and application to ARM measurements. *J. Atmos. Sci.*, **54**, 1503-1524.
- Zhang, M. H., J. L. Lin, R. T. Cederwall, J. J. Yio, and S. C. Xie, 2001: Objective analysis of ARM IOP data: Method and sensitivity. *Mon. Wea. Rev.*, **129**, 295-311.

- Zeng, X., W.-K. Tao, S. Lang, A. Y. Hou, M. Zhang, and J. Simpson, 2008: On the sensitivity of atmospheric ensembles to cloud microphysics in long-term cloud-resolving model simulations. *J. Meteor. Soc. Japan*, **86A**, 45-65.
- Zeng, X., W.-K. Tao, M. Zhang, A. Y. Hou, S. Xie, S. Lang, X. Li, D. Starr, and X. Li, 2009a: A contribution by ice nuclei to global warming. *Quart. J. Roy. Meteor. Soc.*, **135**, 1614-1629.
- Zeng, X., W.-K. Tao, M. Zhang, A. Y. Hou, S. Xie, S. Lang, X. Li, D. Starr, X. Li, and J. Simpson, 2009b: An indirect effect of ice nuclei on atmospheric radiation. *J. Atmos. Sci.*, **66**, 41-61.
- Zeng, X., W.-K. Tao, T. Matsui, S. Xie, S. Lang, M. Zhang, D. Starr, and X. Li, 2011: Estimating the Ice Crystal Enhancement Factor in the Tropics. *J. Atmos. Sci.*, **68**, 1424-1434.
- Zeng, X., W.-K. Tao, T. Matsui, S. Xie, S. Lang, M. Zhang, D. Starr, and X. Li, 2011: Estimating the Ice Crystal Enhancement Factor in the Tropics. *J. Atmos. Sci.*, **68**, 1424-1434.
- Zeng, X., W.-K. Tao, S. Powell, R. A. Houze Jr., P. Ciesielski, N. Guy, H. Pierce, and T. Matsui, 2012: A comparison of the water budgets between clouds from AMMA and TWP-ICE. *J. Atmos. Sci.*, (accepted)
- Zhou, Y., W.-K. Tao, A. Hou, C.-L. Shie, K. -M. Lau, M. -D. Chou, X. Lin, B. Olson, and M. Grecu, 2007: Using High-Resolution Satellite Observations for Evaluation of Cloud and Precipitation Statistics from Cloud-Resolving Model Simulations. Part I: South China Sea Monsoon Experiment. *J. Atmos. Sci.*, **64**, 4309-4329.
- Zipser, E. J., R. J. Meitin, and M. A. LeMone, 1981: Mesoscale motion fields associated with a slowly moving GATE convective band. *J. Atmos. Sci.*, **38**, 1725-1750.
- Zipser, 2003: Some views on 'Hot Towers' after 50 years of tropical field programs and two years of TRMM data. *AMS Meteorological Monographs - Cloud Systems, Hurricanes and TRMM*, **29**, 49-58.

	Required TRMM data	Algorithm products	Key references in algorithm description	Algorithm developers
CSH (Convective-Stratiform Heating)	PR, TMI, PR-TMI	Q_1 , LH, Q_2	Tao <i>et al.</i> (1990, 1993, 2000, 2001, 2010)	W.-K. Tao & S. E. Lang
SLH (Spectral Latent Heating)	PR	LH, Q_1 - Q_R , Q_2	Shige <i>et al.</i> (2004, 2007, 2008, 2009)	S. Shige & Y. N. Takayabu
TRAIN (Trained Radiometer Algorithm)	TMI (PR training)	Q_1 - Q_R , LH	Grecu and Olson (2006), Olson <i>et al.</i> (2006) Grecu <i>et al.</i> (2009)	M. Grecu & W. Olson
HH (Hydrometeor Heating)	PR-TMI	LH	Yang <i>et al.</i> (1999, 2006)	E. A. Smith & Y. Song
PRH (Precipitation Radar Heating)	PR	LH	Satoh and Noda (2001)	S. Satoh & A. Noda

Table 1 Summary of the five LH algorithms (see Tao et al. 2006 for further details and salient references). Data inputs, retrieved products, and salient references are included. The conventional relationship between Q_1 (apparent heat source), LH, and Q_R (radiative heating) is expressed by $Q_1 - Q_R = LH + EHT$, where the final term represents eddy heat transport by clouds (vertically integrated EHT is zero, i.e., it provides no explicit influence on surface rainfall). TMI is the TRMM Microwave Imager and PR the TRMM precipitation radar.

Field experiment	Location	Period	Reference
GATE	Tropical Atlantic	26 June – 19 September 1974	Houze and Betts (1981)
TOGA-COARE	Equatorial West Pacific	1 November 1992 – 28 February 1993	Webster and Lucas (1992)
SCSMEX (N & S)	South China Sea	2-25 May and 5-22 June 1998	Lau <i>et al.</i> (2000)
LBA	Amazonia	1 November 1998 – 28 February 1999	Silva Dias <i>et al.</i> (2005)
KWAJEX	Marshall Islands	24 July – 15 September 1999	Yuter <i>et al.</i> (2005)
TWP-ICE	Darwin	21 January – 12 February 2006	May <i>et al.</i> (2008)
MISMO	Equatorial Indian Ocean	24 October – 25 November 2006	Yoneyama <i>et al.</i> (2008)

Table 2 Location, duration and references of field campaigns. One of the major objectives of SCSMEX, KWAJEX and LBA was to provide forcing for CRMs and validation for TRMM LH profiles.

Field campaign	Simulated rainfall amount (mm/day)	Stratiform rain percentage (%)	Estimated rainfall amount (mm/day)
SCSMEX (NESA)	12.31	42.6	11.35
ARM (1997)	4.31	41.3	4.32
ARM (2002)	4.85	36.0	4.77
TOGA COARE (1992-1993)	7.72	47.6	9.32
GATE (1974)	10.56	41.4	11.38

Table 3 CRM-simulated rainfall amount and stratiform % for SCSMEX (1998), ARM (1997, 2002), TOGA COARE (1992) and GATE (1974). Adapted from Tao et al. (2010).

Case	CSH (Q1)	HH (LH)	TRAIN (Q1, Q1-QR)	SLH (Q1-QR, LH)	PRH (LH)	Diagnostic (Q1)
SCSMEX - NESA	6.6	6.6	6.5, 6.6	7.5, 7.5	6.5	7.6, 7.7
SCSMEX - SESA	7.5	6.6	6.7, 6.6	7.6, 7.6	6.0	6.5, 6.7
KWAJEX	6.7	5.5	na , 3.6 / 6.5 (2 max)	7.5, 7.5	6.6	4.5
ARM – Spring 2000	7.0	3.0	na	5.5, 5.6	4.5	6.0
ARM - Summer 2002	6.5	5.5	na	5.6, 5.6	5.6	8.1

Table 4 Altitude of maximum mean heating in km. Diagnostic Q_I is calculated from both within the associated sounding arrays and the gridded rectangular study areas for the two SCSMEX cases but only for the associated sounding arrays for KWAJEX and ARM.

Authors	Topic/Title
T. L'Ecuyer and G. McGarragh	A 10-Year Climatology of Tropical Radiative Heating and Its Vertical Structure from TRMM Observations
S. Shige, Y. N. Takayabu, S. Kida, W.-K. Tao, X. Zeng, C. Yokoyama, and T. L'Ecuyer	Spectral Retrieval of Latent Heating Profiles from TRMM PR Data. Part IV: Comparisons of Lookup Tables from Two- and Three-Dimensional Cloud-Resolving Model Simulations
M. Grecu, W. Olson, C.-L. Shie, T. L'Ecuyer, and W.-K. Tao	Combining Satellite Microwave Radiometer and Radar Observations to Estimate Atmospheric Heating Profiles
W.-K. Tao, S. Lang, X. Zeng, S. Shige, and Y. N. Takayabu	Relating Convective and Stratiform Rain to Latent Heating
T. Krishnamurti, A. Chakraborty, and A. K. Mishra	Improving Multimodel Forecasts of the Vertical Distribution of Heating using the TRMM Profiles
X. Jiang, D. Waliser, W. Olson, W.-K. Tao, T. L'Ecuyer, J.-L. Li, B. Tian, Y. L. Yung, A. Tompkins, S. Lang, , and M. Grecu	Vertical Heating Structures Associated with the MJO as Characterized by TRMM Estimates, ECMWF Reanalyses, and Forecasts: A Case Study during 1998/99 Winter
S. Hagos, C. Zhang, W.-K. Tao, S. Lang, B. Olson, Y. Takayabu, S. Shige, M. Katsumata and T. L'Ecuyer	Estimates of Tropical Diabatic Heating Profiles: Commonalities and Uncertainties
K.-M. Lau and H.-T. Wu	Characteristics of Precipitation, Cloud, and Latent Heating Associated with the Madden-Julian Oscillation
M. Zuluaga, C. Hoyos, and P. Webster	Spatial and Temporal Distribution of Latent Heating in the South Asian Monsoon Region
Y. N. Takayabu, S. Shige, W.-K. Tao and N. Hirota	Shallow and Deep Latent Heating Modes over Tropical Oceans Observed with TRMM PR Spectral Latent Heating Data
Y.-M. Kodama, M. Katsumata, S. Mori, S. Sato, Y. Hirose, and H. Ueda	Climatology of Warm Rain and Associated Latent Heating Derived from TRMM-PR observations
S. Xie, T. Hume, C. Jakob, S. A. Klein, R. B. McCoy and M. Zhang	Observed Large-Scale Structures and Diabatic Heating and Drying Profiles during TWP-ICE
R. H. Johnson, P. E. Ciesielski, T. S. L'Ecuyer, and A. J. Newman	Diurnal Cycle of Convection During the 2004 North American Monsoon Experiment

Table 5 Authors and titles of papers published in the special collection on TRMM diabatic heating in the *J. of Climate*. Dr. Tony Del Genio was a guest editor for this special collection.

Phase	Lifecycle	Tb (K°)	ETH (km)	Types of cloud system
1-2	Genesis	290-300	2.5-4.5	Abundant occurrence of WL
3-4	Developing	260-280	4.5	Large increase of MM and CM
5	Mature or peak convection	< 275	> 5	Large increase of CM and CH
6	Start of decaying	Wide range of Tbs	> 5	
7	Decaying	< 275	> 6-7	Increase of WL
8	Similar to phase 1	290-300	2.5-4.5	WL

Table 6 The characteristics of MJO phases in terms of brightness temperature (Tb), echo top height (ETH), and type of cloud systems. WL stands for warm-rain low-level cloud, MM for mixed-phase rain, middle-level cloud, CM for cold cloud-top and medium storm height, and CH for cold rain, high-cloud.

Experiment	Cumulus parameterization scheme	Microphysics scheme
Model1	Kain-Fritsch (Kain 2004))	Kessler (Kessler 1969)
Model2	Betts-Miller-Janjic (Janjic 1994, 2000)	Kessler
Model3	Grell-Devenyi ensemble (Grell and Devenyi 2002)	Kessler
Model4	Kain-Fritsch	WSM5 (Hong <i>et al.</i> 2004)
Model5	Betts-Miller-Janjic	WSM5
Model6	Grell-Devenyi ensemble	WSM5

Table 7 Numerical experiments conducted by different combinations of cumulus parameterization and microphysics schemes.

	Spatial scale	Temporal scale	Algorithm	Products
Gridded	0.5 x 0.5 degrees 19 vertical layers	Monthly	SLH-PR CSH-Combined	LH, Q1-QR, Q2 LH, Q1, QR, Q2
Orbital*	Pixel 19 vertical layers	Instantaneous	SLH-PR CSH-Combined	LH, Q1-QR, Q2 LH, Q1, QR, Q2
Gridded Orbital	0.5 x 0.5 degrees 19 vertical layers	Instantaneous w/ time stamps on each grid	SLH-PR CSH-Combined	LH, Q1-QR, Q2 LH, Q1, QR, Q2

Table 8 Summary of PMM cloud heating products from the CSH and SLH algorithms.
*Orbital heating is not a standard PMM product.

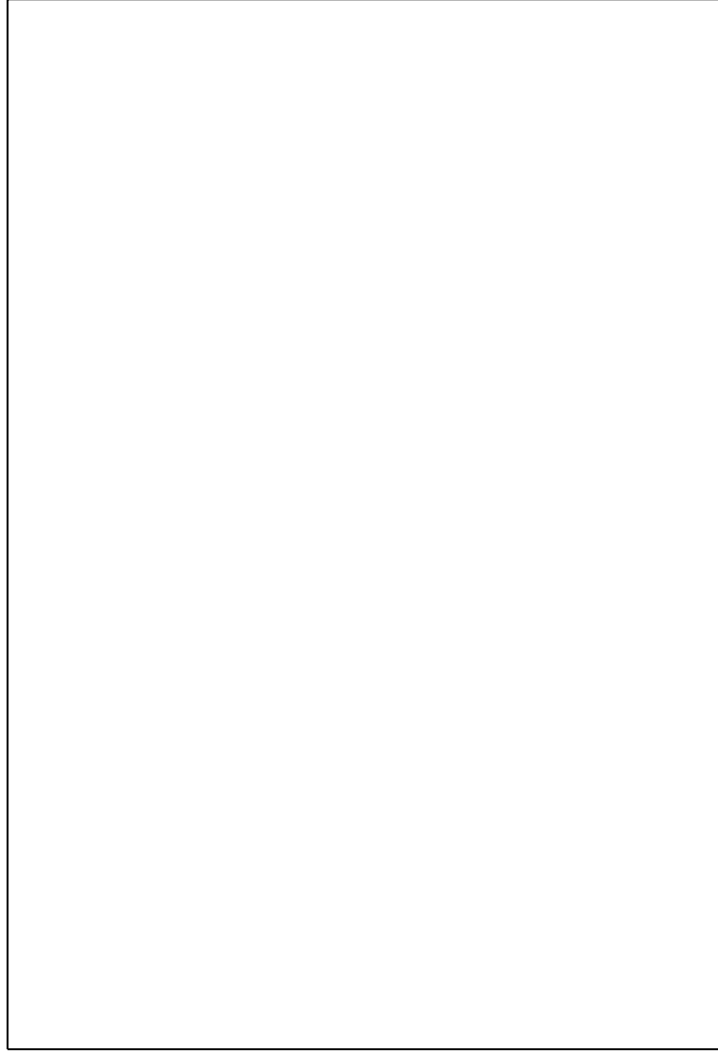


Fig. 1 Goddard Cumulus Ensemble model (GCE)-simulated time mean profiles of LH components averaged over the **(a)** convective region and **(b)** stratiform region. The components consist of condensation (solid red), evaporation (solid blue), deposition (dashed red), sublimation (dashed blue), freezing (solid orange), melting (solid turquoise), and total (solid black).

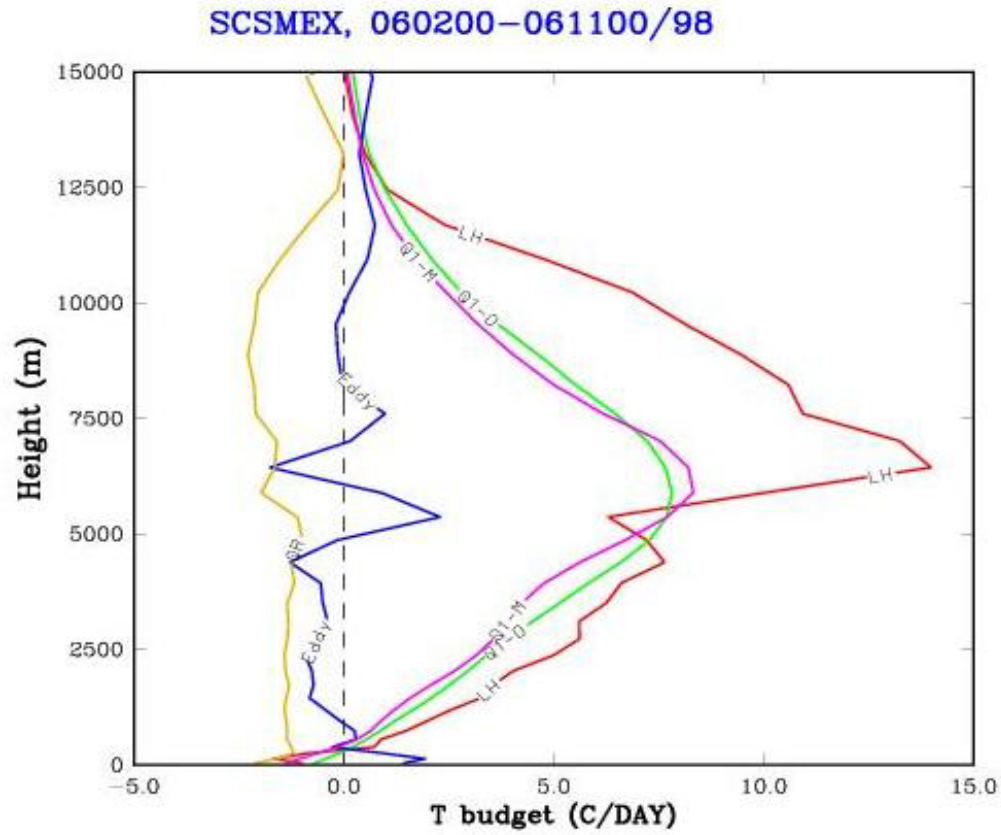


Fig. 2 GCE-simulated time-domain mean profiles of net condensation or LH (c-e+d-s+f-m, red), eddy heat flux divergence (blue), Q_R (yellow) and Q_1 (purple). The observed Q_1 (green) estimated from a sounding network is also shown for comparison. Adapted from Tao (2007).

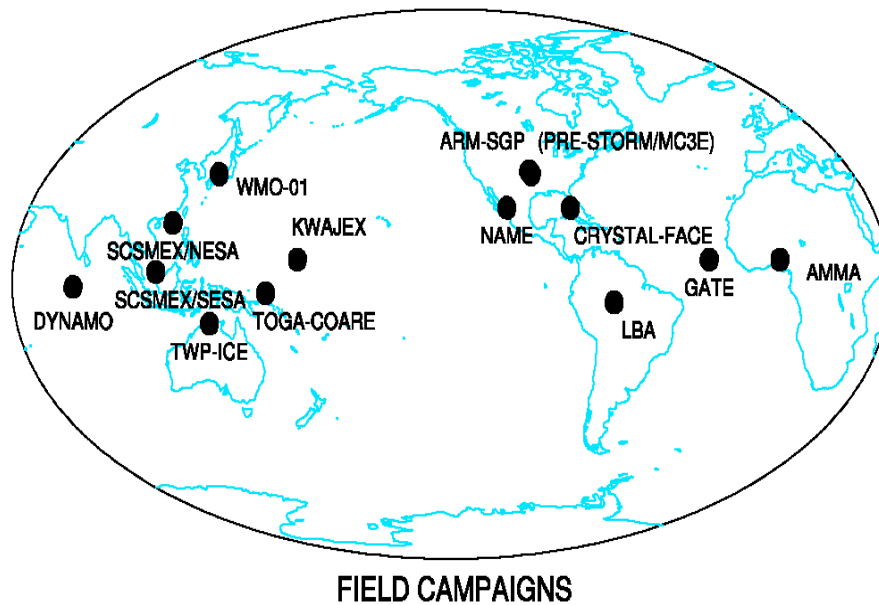


Fig. 3 Geographic locations of twelve field campaigns used to provide data to drive and evaluate CRM simulations. These include: the ARM-SGP (Southern Great Plains) campaigns conducted in the summer of 1997, the spring of 2000 and the summer of 2002, GATE (1974), KWAJEX (1999), TOGA COARE (conducted in 1992 and 1993), TWP-ICE (2006, the Tropical Warm Pool – International Cloud Experiment), and SCSMEX/NESA and SESA (1998, northern and southern enhanced sounding arrays, respectively), AMMA (2006, the African Monsoon Multidisciplinary Analysis), MC3E (2011, the Midlatitude Continental Convective Clouds Experiment) and AMIE/DYNAMO (2011, the ARM MJO Investigation Experiment/Dynamics of the MJO). MISMO has the same location as DYNAMO.

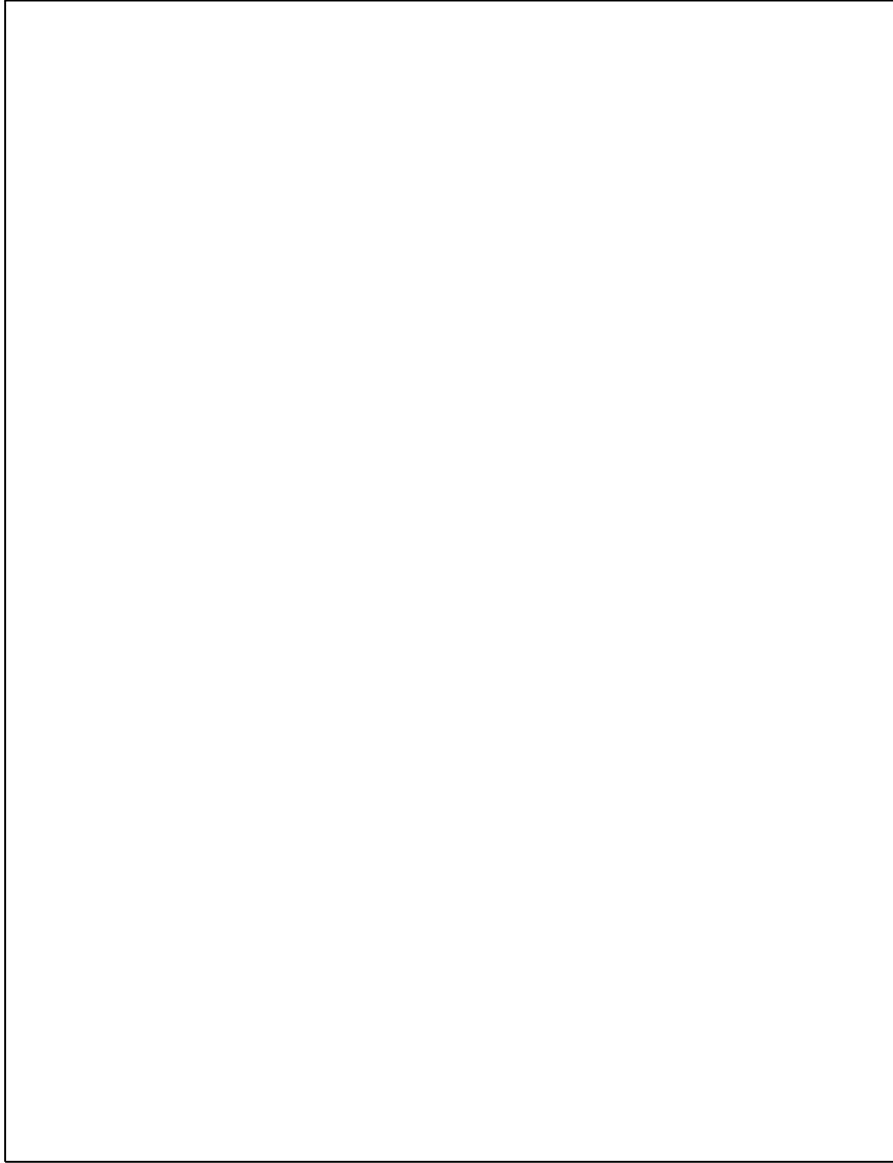


Fig. 4 Evolution of LH profiles (5-min intervals) over the TOGA COARE IFA for an 8-day period (19-27 December 1992) from: **(a)** GCE simulation, **(b)** SLH algorithm reconstruction (middle panel), and **(c)** CSH algorithm reconstruction (lower panel). The contour interval is $5^{\circ}\text{C day}^{-1}$. GCE-simulated convective/shallow-stratiform/anvil stratus fractions, surface rain rates (RRs), PTHs, and melting level RRs are used as inputs to the SLH algorithm with profiles averaged over a 512 km grid mesh. Adapted from Shige *et al.* (2004).

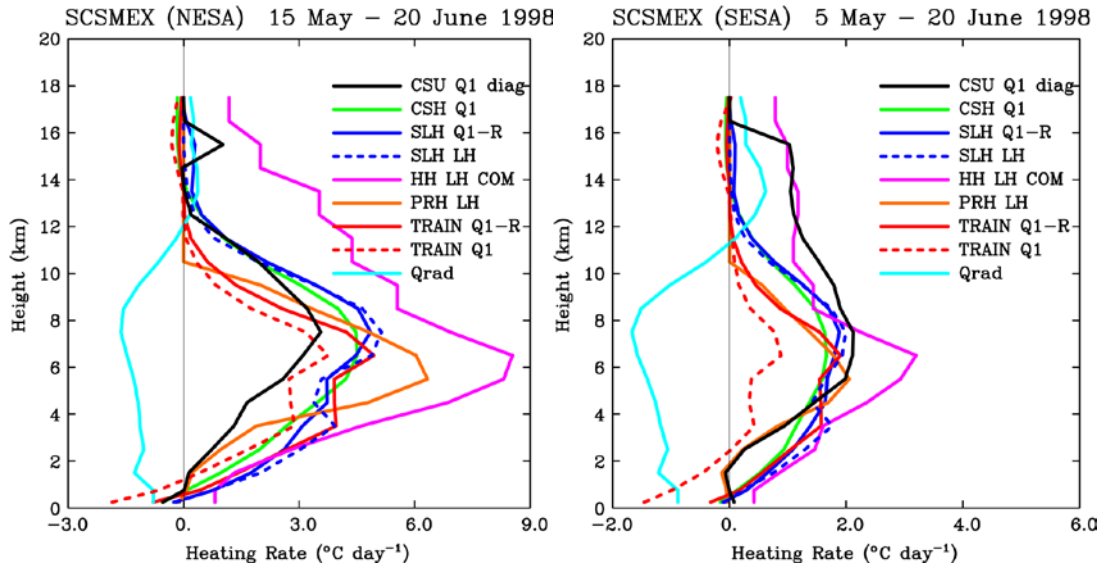


Fig. 5 Space/time-averaged heating profiles for the Case 1a (SCSMEX-NESA, left panel) and Case 1b (SCSMEX-SESA, right panel) regions. Profiles for different heating terms are obtained from five different satellite algorithms: solid green lines from CSH, solid violet lines from HH, solid red and dashed red lines from TRAIN and TRAIN + L'Ecuyer's Q_R , respectively, solid blue and dashed blue lines from SLH, and solid orange lines from PRH. Q_1 profiles from CSU's diagnostic calculations are the solid black lines (DIAG) from within the NESA/SESA sounding networks. Satellite-derived Q_R profiles from CSU (solid turquoise lines, Qrad), are a gridded product.

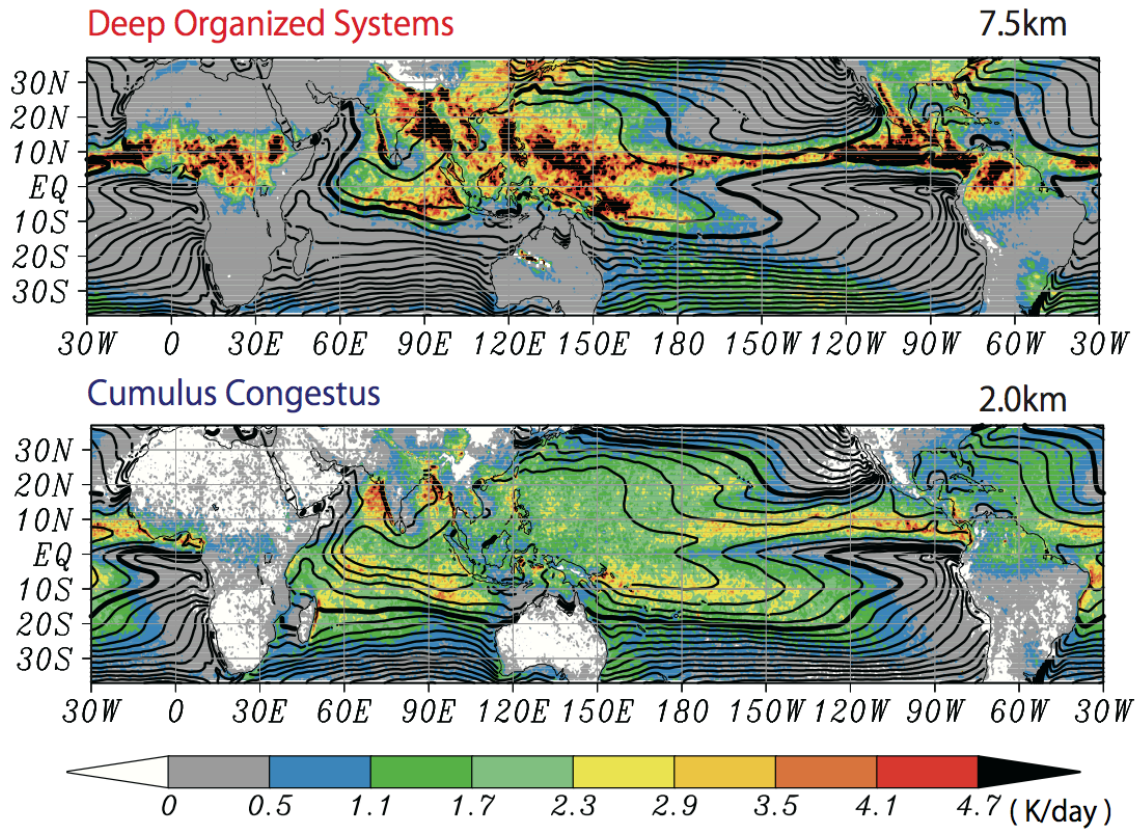


Fig. 6 $Q_I - Q_R$ at 7.5 km (a) and 2.0 km (b) averaged for June-August from 1998 to 2007 overlaid on SST (contours). Color scale labels show $Q_I - Q_R$ values in degrees day⁻¹; SST contour intervals are every 1 °C with the 28 °C and 25 °C contours shown in thick lines in the upper and lower panels, respectively. Adapted from Takayabu *et al.* (2010).

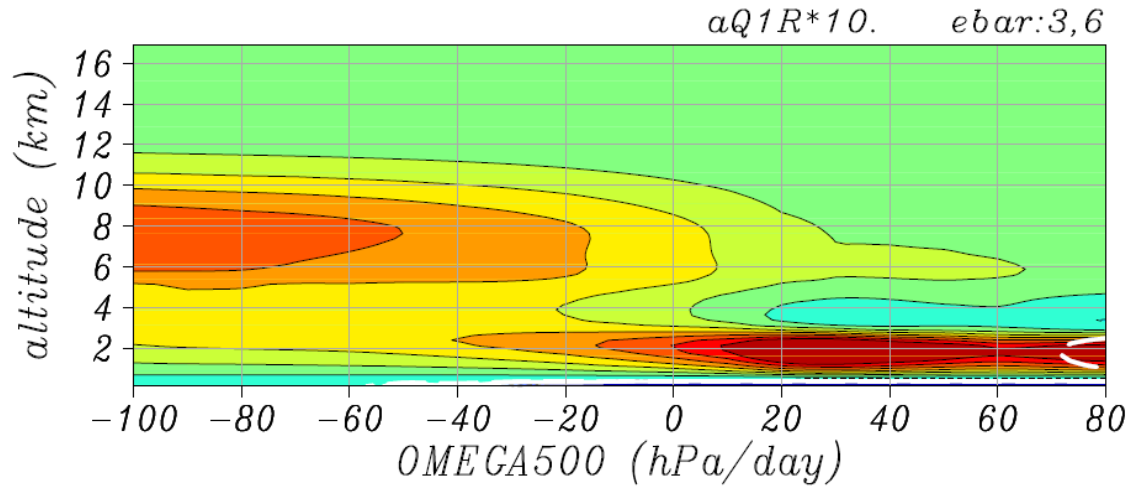


Fig. 7 Seven-year conditional mean Q_I - Q_R profiles stratified with vertical velocity (dp/dt) at 500 hPa averaged for September-November from 30N-30S at all longitudes over the ocean in association with all rain. The values for the color scale are scaled by a factor of 10. Adapted from Takayabu *et al.* (2010).

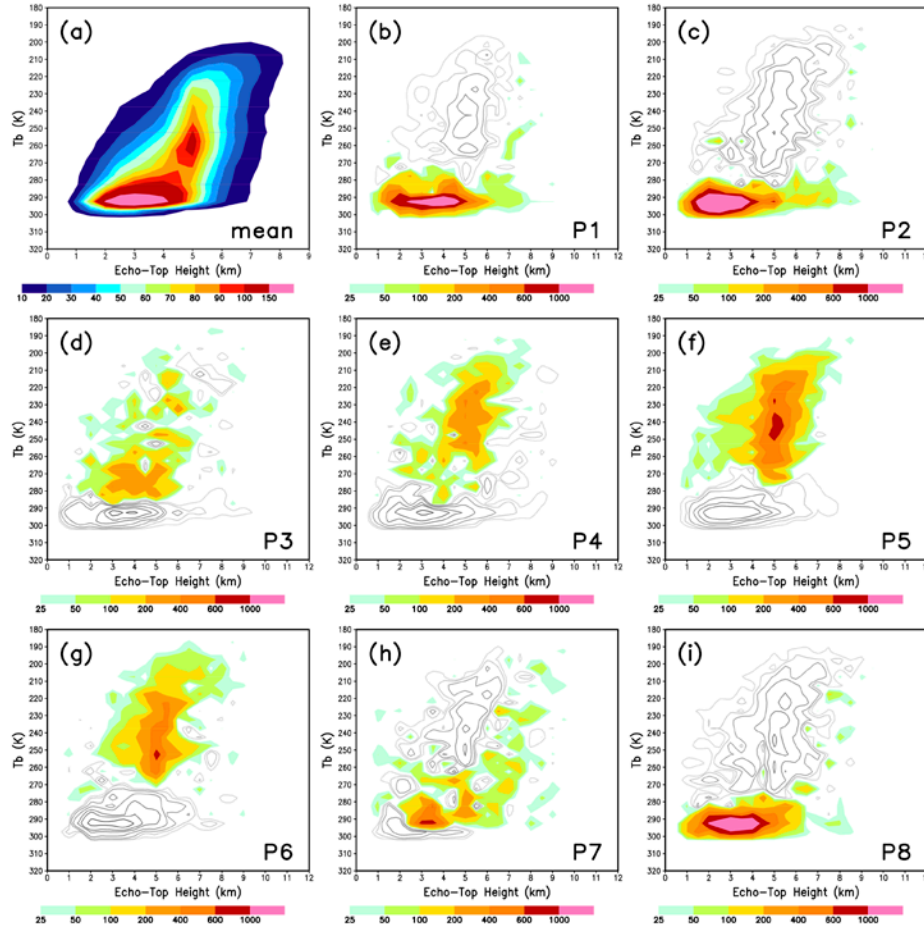


Fig. 8 Joint PDF (JPDF) of Tb and ETH over the equatorial western Pacific: (a) mean state of the eight MJO phases and (b)–(i) the difference between the JPDF for each of the 8 phases (P1–P8) and the mean state. Positive values are color shaded and negative values are contoured. The units for the mean state are in 0.01% of the total occurrence counts. For P1–P8, the units are number of counts. Adapted from Lau and Wu (2010).

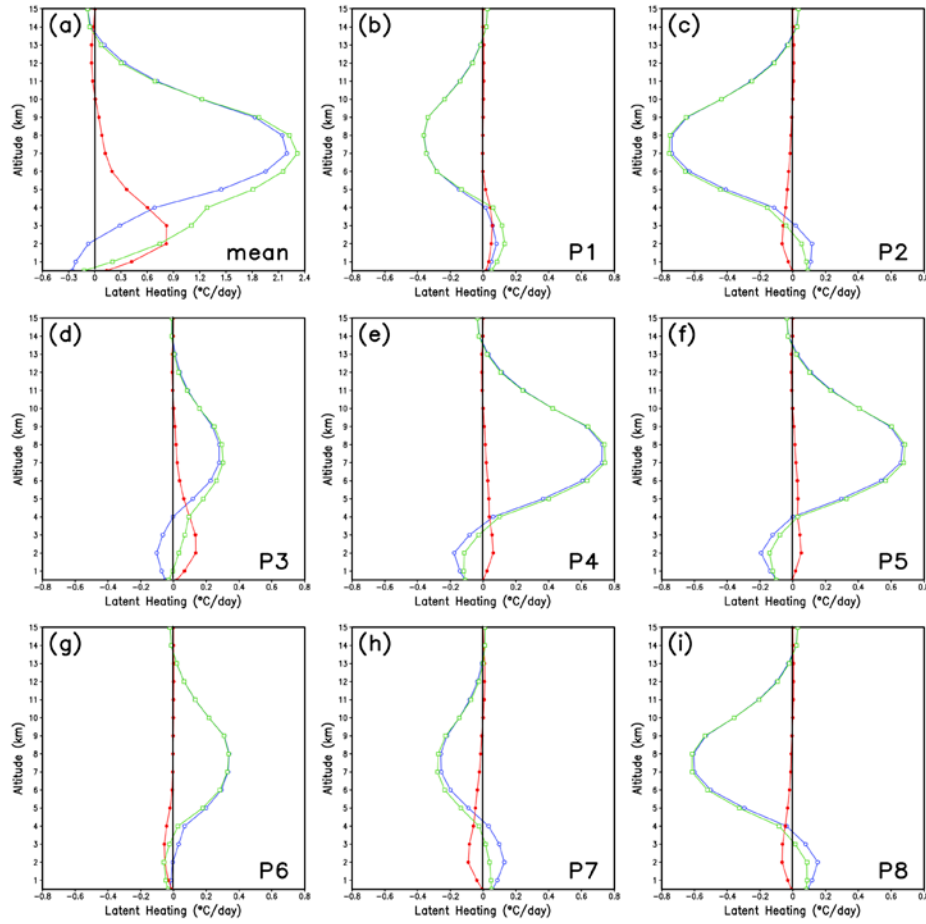


Fig. 9 MJO LH profiles based on the CSH algorithm and daily averaged ETH: (a) mean state of the eight MJO phases and (b)–(i) the difference between the heating profile of each phase, P1–P8, and the mean state. The three curves in each panel are red for ETHs < 5 km, blue for ETHs > 5 km, and green for total. Adapted from Lau and Wu (2010).

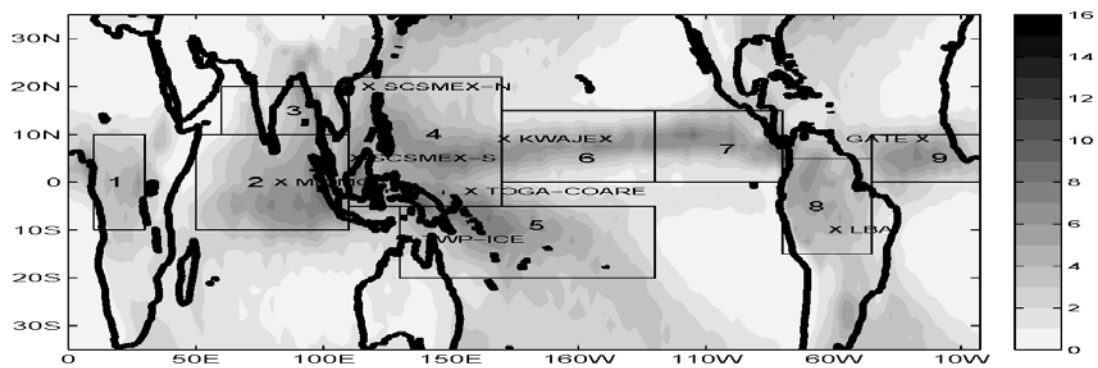


Fig. 10 Ten-year mean precipitation from TRMM (3G68, mm/day). Boxes indicate the analysis domains. Locations of the field campaign sounding sites are marked by an 'X'. Adapted from Hagos *et al.* (2010).

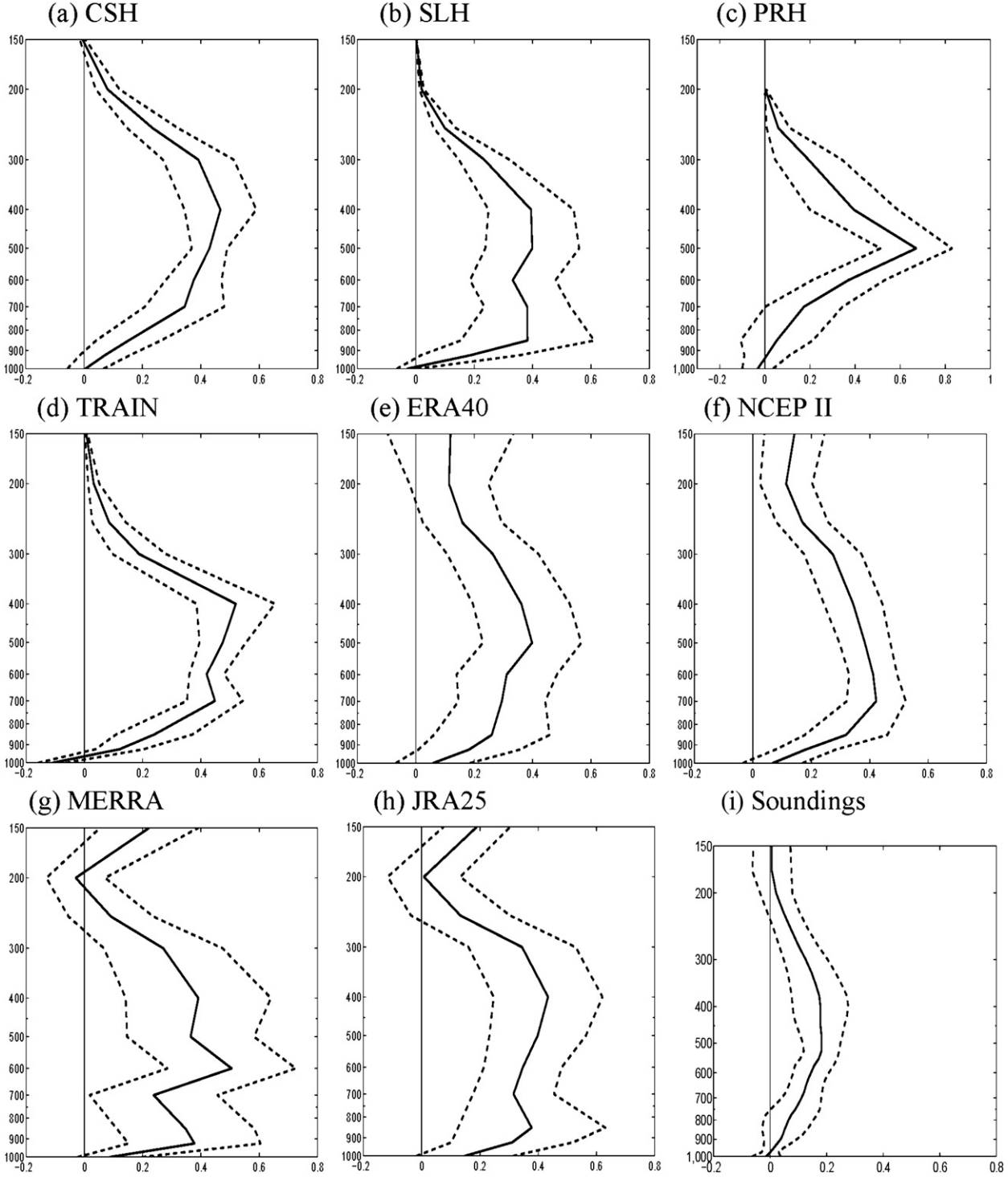


Fig. 11 **(a)–(h)** Normalized mean heating profiles averaged over the tropical precipitation regions (shown by the boxes in Fig. 10) and **(i)** the mean profile of the diabatic heating from all the soundings. The normalization was done by dividing each heating profile by its norm, which is the square root of the sum of the squared heating at all levels. Dashed lines are the standard deviation. Adapted from Hagos *et al.* (2010).

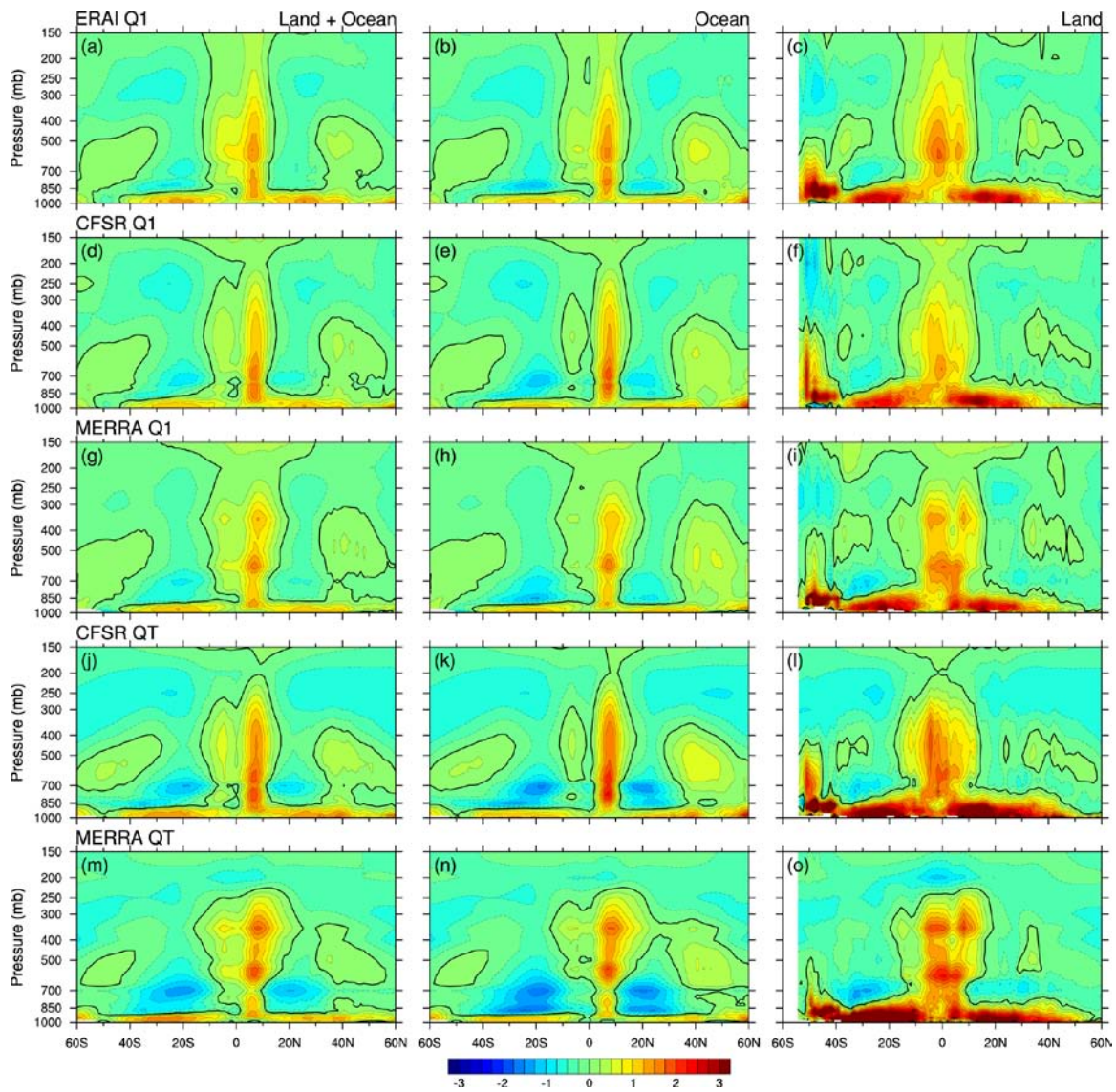


Fig. 12 Time and zonal means of diabatic heating (K day^{-1}) from (top to bottom row) ERAI Q₁, CFSR Q₁, MERRA Q₁, CFSR Q_T and MERRA Q_T (left column) and over the oceans (middle) and land (right) only. Adapted from Ling and Zhang (2012).

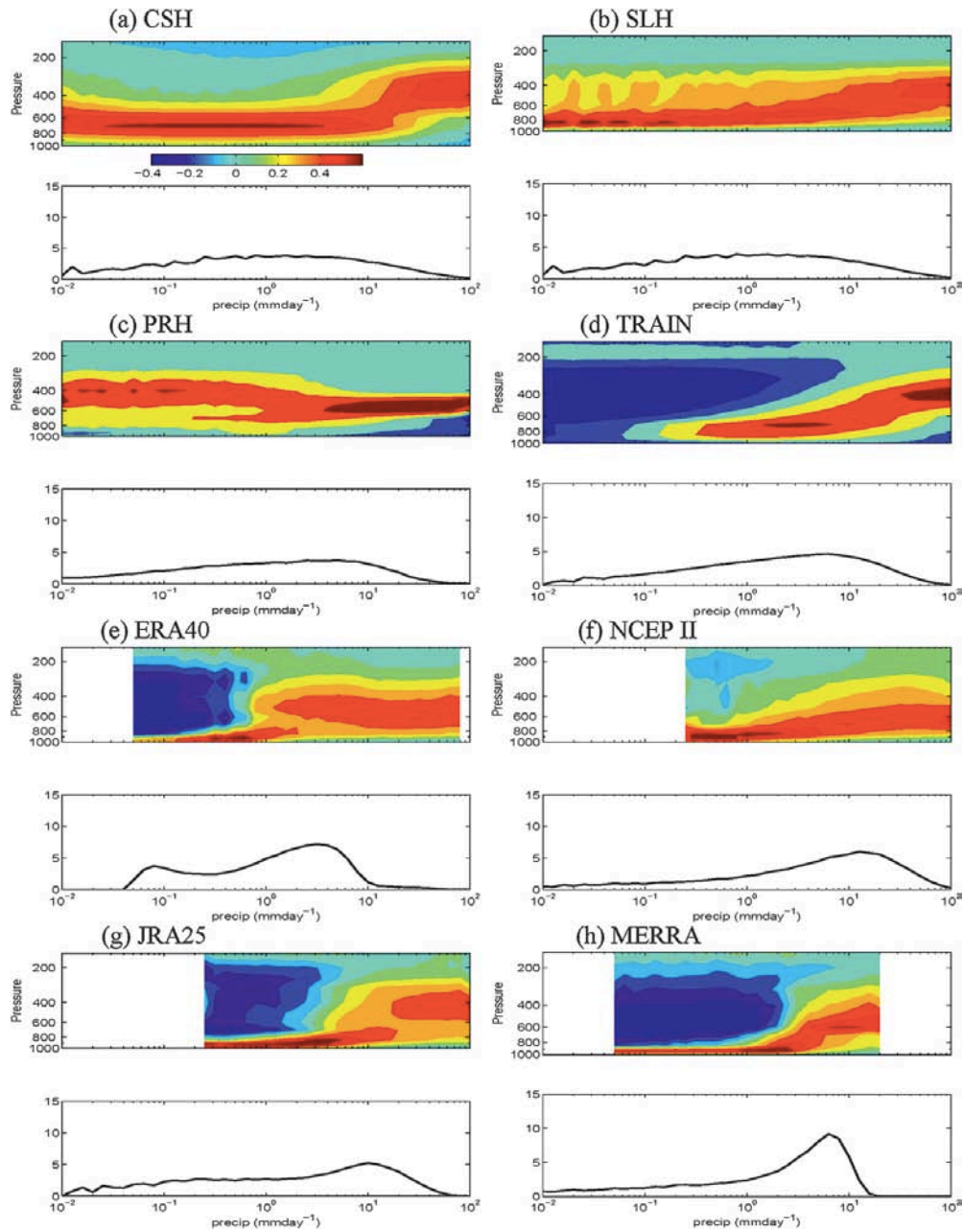


Fig. 13 Normalized LH profiles as functions of precipitation intensity (in units of standard deviation) and the PDF of precipitation over the Atlantic. The dashed lines indicate a precipitation rate of 1 mm/day. For the soundings, vertically-integrated diabatic heating is used as a proxy for precipitation. Adapted from Hagos *et al.* (2010).

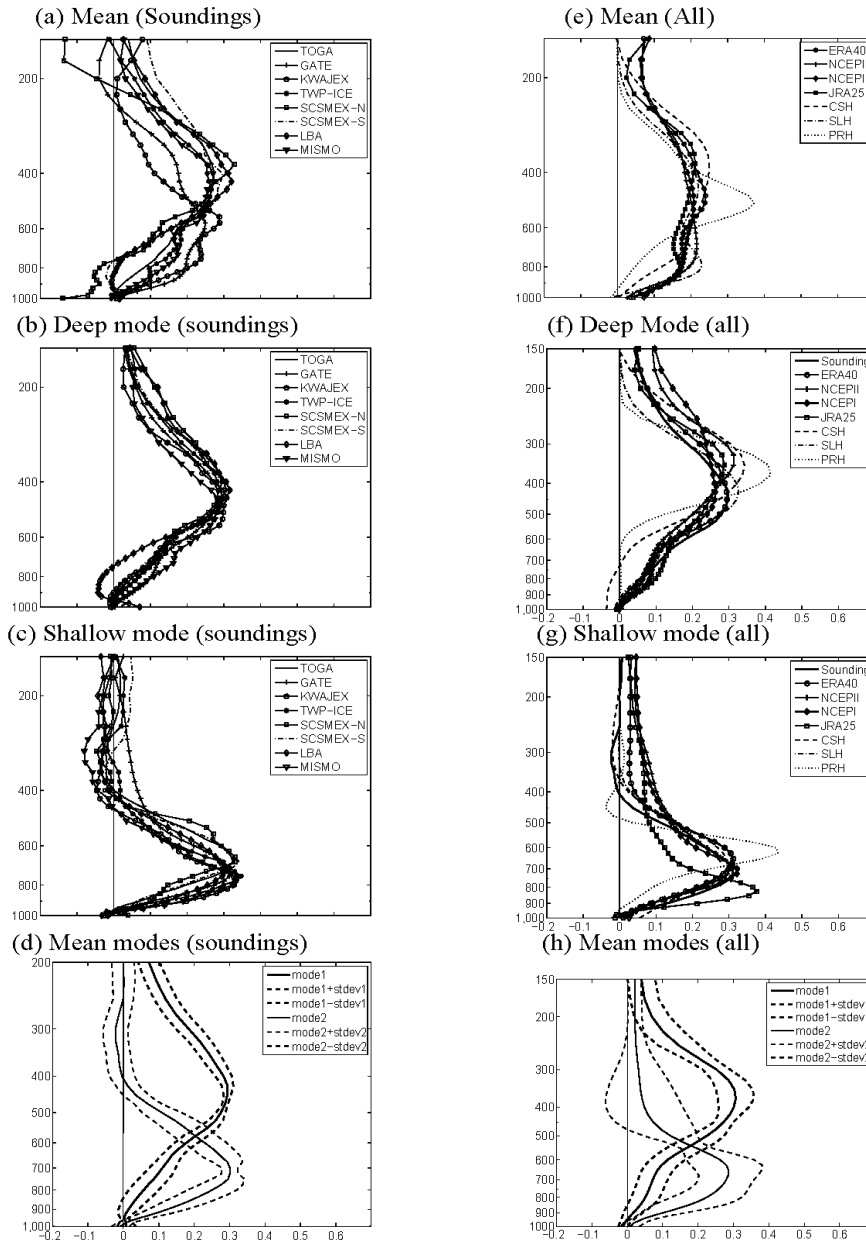


Fig. 14 (a) Mean, (b) deep, (c) shallow, and (d) the average of the deep and shallow mode profiles and their standard deviations from the soundings. (e)-(h) same as (a)-(d) but for the reanalyses and TRMM products. Adapted from Hagos *et al.* (2010).

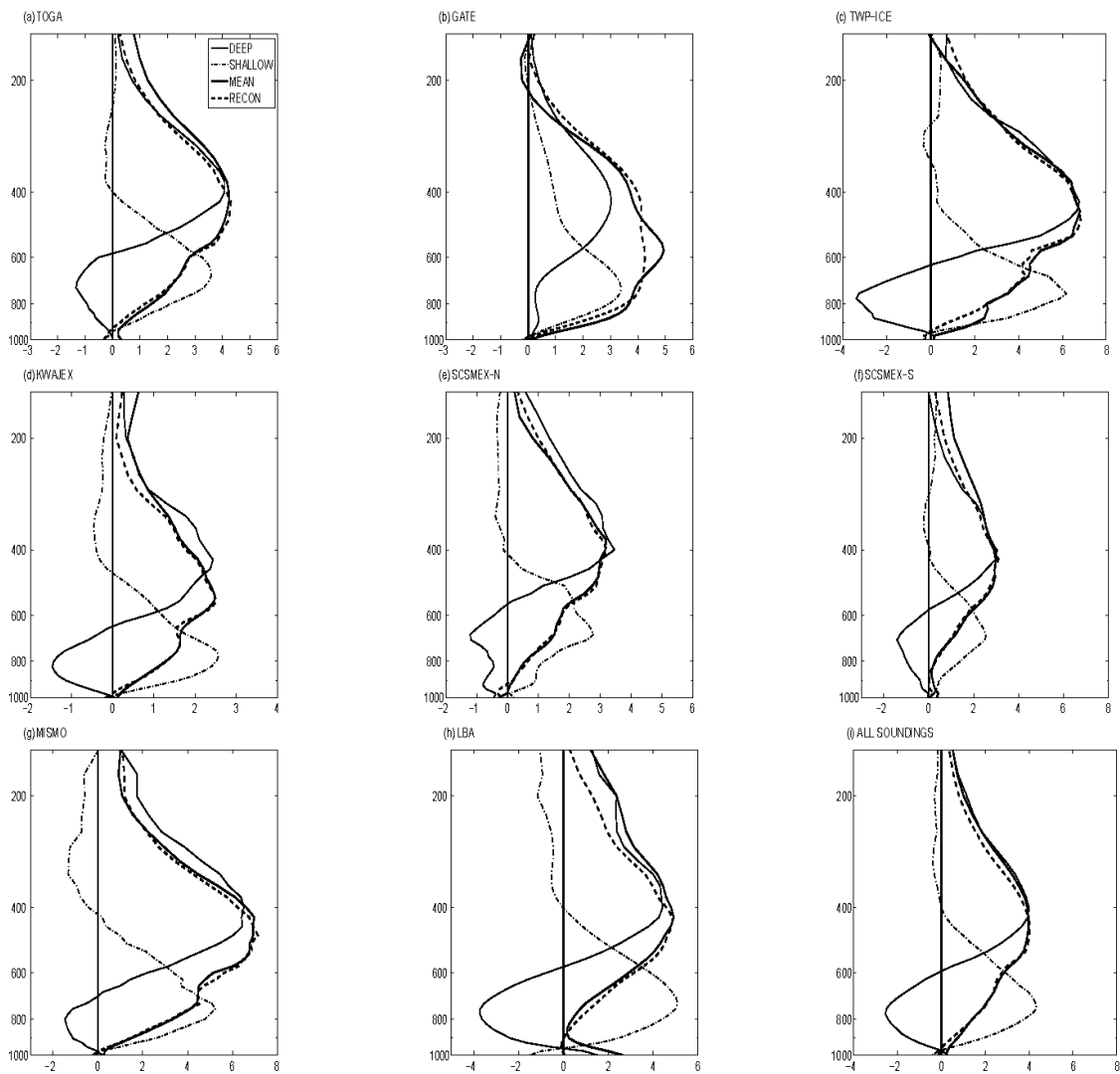


Fig. 15 Reconstruction of mean sounding profiles using the first two oblique rotated EOFs. Adapted from Hagos *et al.* (2010).

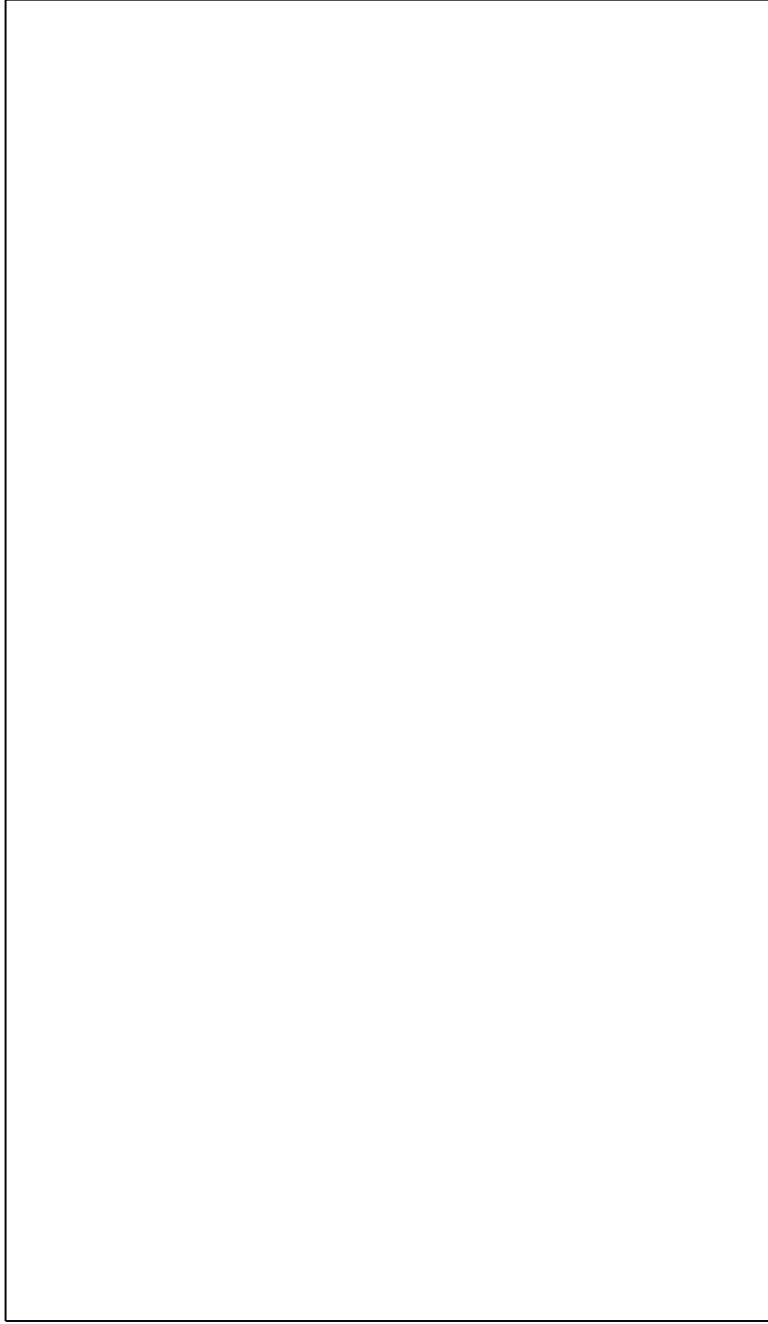


Fig. 16 Vertical-temporal (MJO phase) evolution of anomalous heating Q_1 or Q_1-Q_R for TRMM SLH (shaded, in K day^{-1}) over the WP ($150\text{-}160^\circ\text{E}$, panels a-f) and the EEIO ($80\text{-}90^\circ\text{E}$, panels g-l) based on three reanalysis datasets and three TRMM estimates. The black curve in each panel represents the evolution of TRMM 3B42 rainfall anomalies (see scales on right y-axis in units of mm day^{-1}). All variables are averaged over $10^\circ\text{S}\text{-}10^\circ\text{N}$. Adapted from Jiang *et al.* (2011).

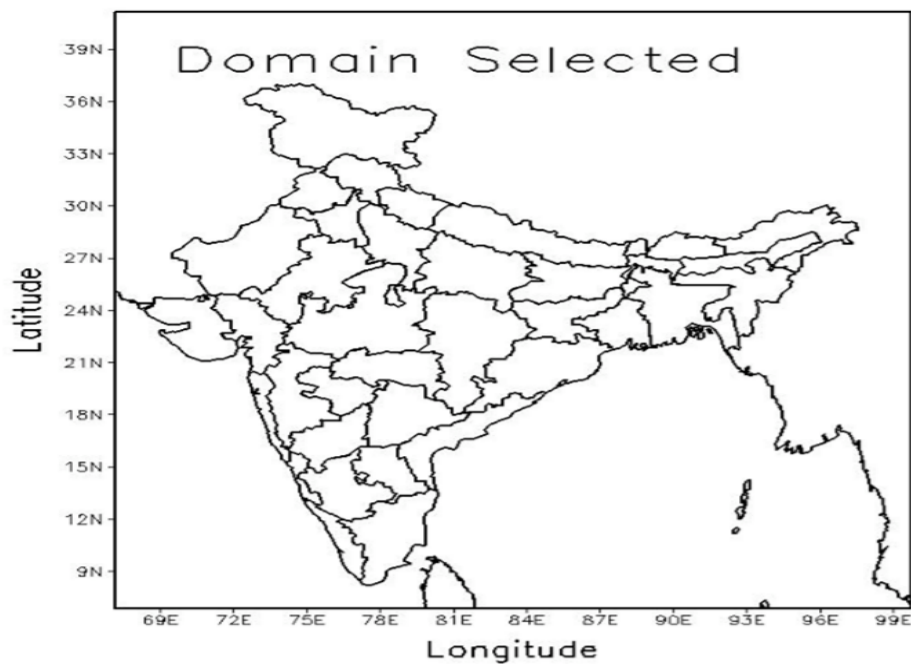


Fig. 17 WRF model configuration used in the mesoscale super ensemble study (6.85-38.01 °N, 67.13-99.27 °E). The horizontal domain resolution is 25 km, and the time step is 100 seconds.

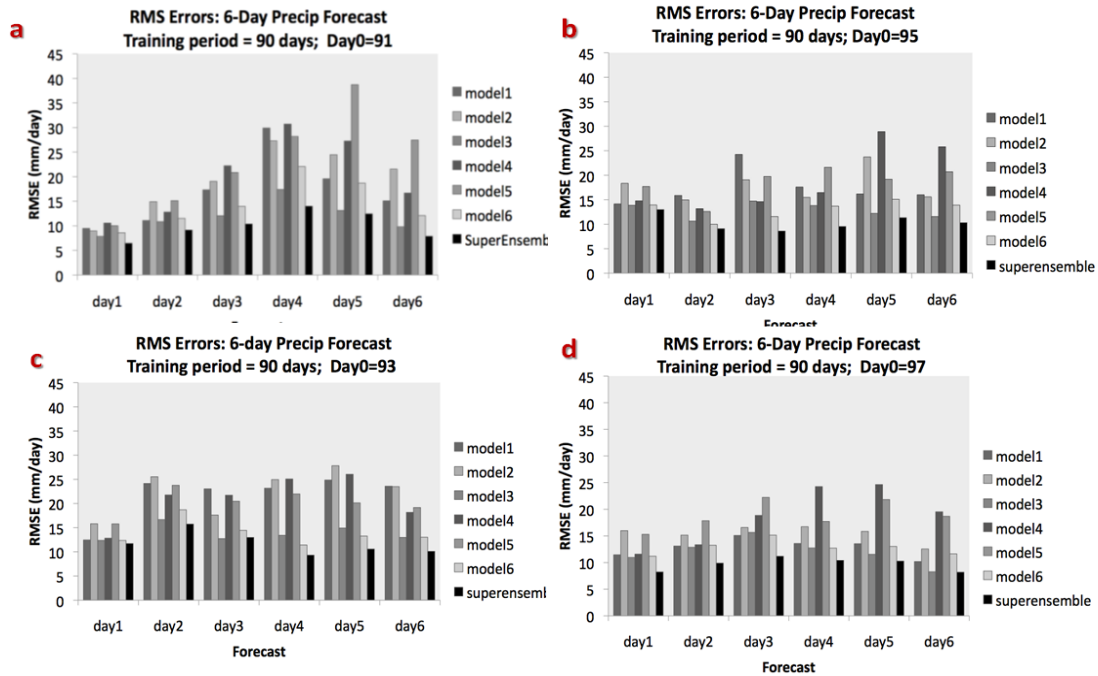


Fig. 18 Comparison of RMS errors for forecasts from the super ensemble and six member models over 6 days with initial conditions at (a) Day0=91, (b) Day0=93, (c) Day0=95, and (d) Day0=97. “Day” refers to forecast days after 90 days of training and Day0 the start day of the forecast. The 91st day is 29 August 2005.

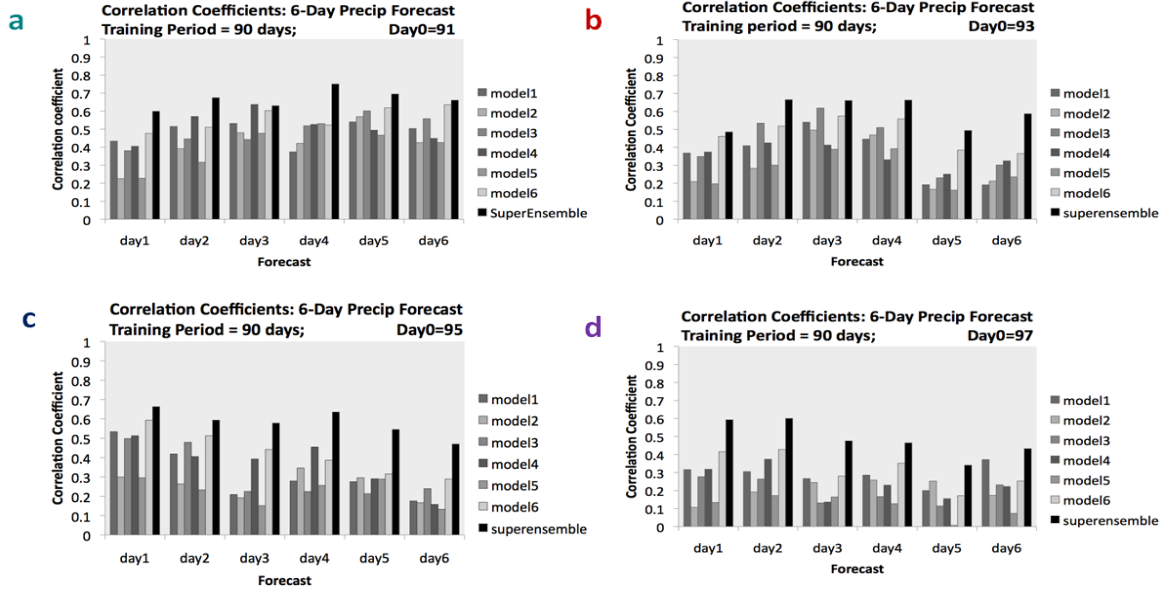


Fig. 19 Comparison of spatial correlation coefficients between observed and simulated rain for forecasts from the super ensemble and six member models over 6 days with initial conditions at (a) Day0=91, (b) Day0=93, (c) Day0=95, and (d) Day0=97. “Day” refers to forecast days after 90 days of training and Day0 the start day of the forecast. The 91st day is 29 August 2005.

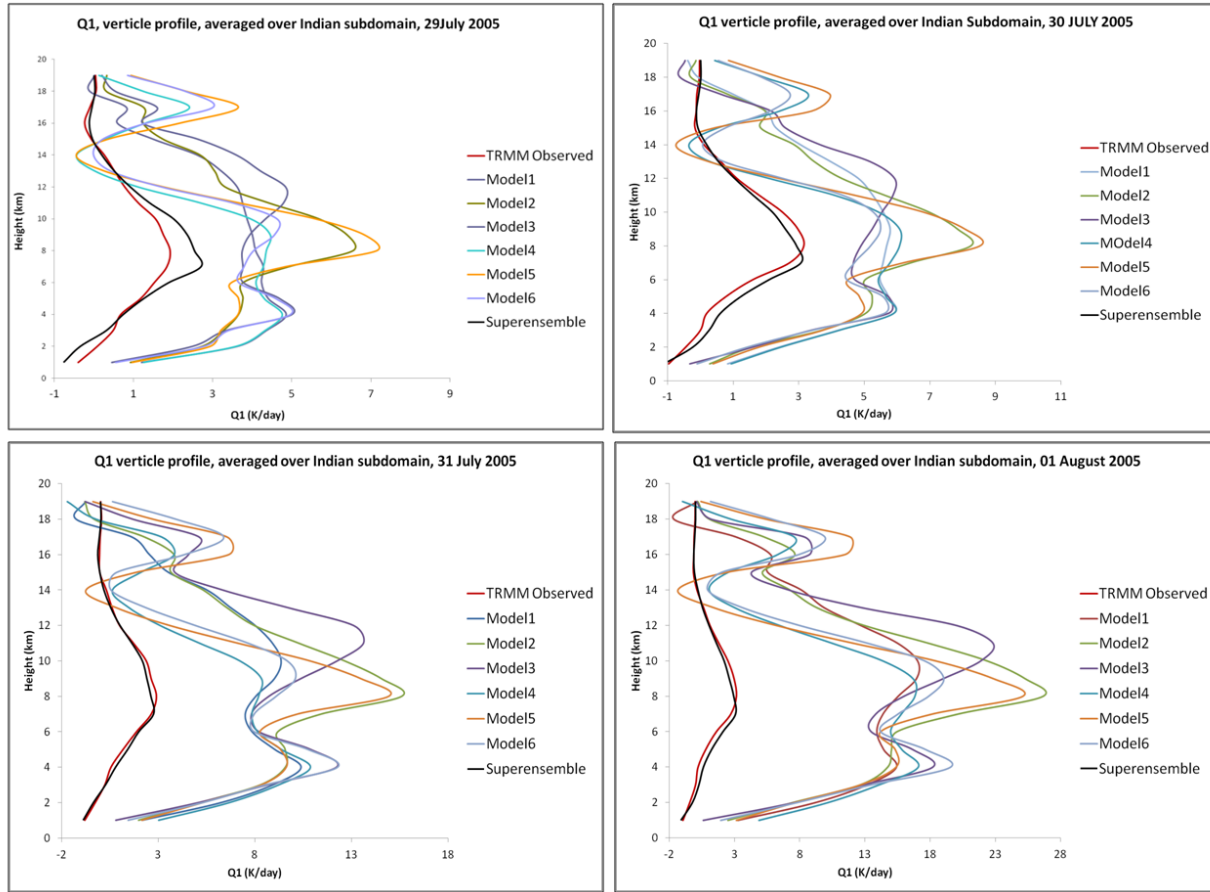


Fig. 20 Forecasts of the vertical distribution of heating Q_1 (K/day) from 6 mesoscale models, the multi-model super ensemble and the satellite-based CSH algorithm over the Indian subdomain (70°E - 90.17°E , 6.85°N - 25.13°N). The respective panels show forecasts in sequence for days 1 through 4.

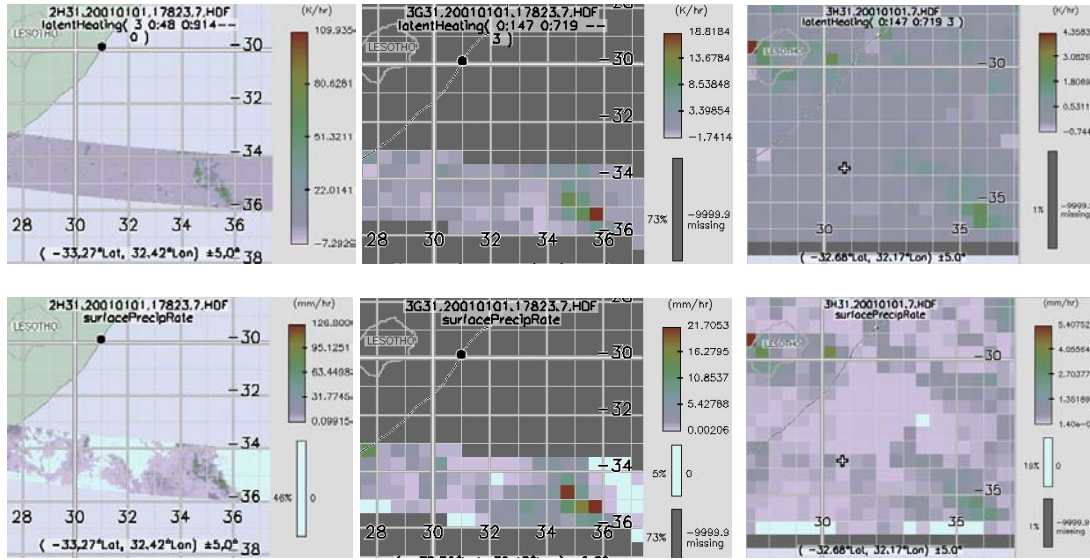


Fig. 21 LH products (top row) from the version 2 CSH algorithm based on rainfall data from the TRMM Combined Algorithm: (left) instantaneous pixel scale LH off the southeast coast of Africa 1 January 2001 at a height near 2.5 km from the orbital product, (center) same but for the 3G31 gridded (0.5 x 0.5 deg) orbital product, and (right) same but for monthly mean LH from the 3H31 gridded monthly product. The new CSH algorithm uses conditional rain rates and LUTs based on GCE results divided into fine intensity and stratiform bins (Tao et al. 2010). The corresponding surface rainfall is shown below each of the LH products.

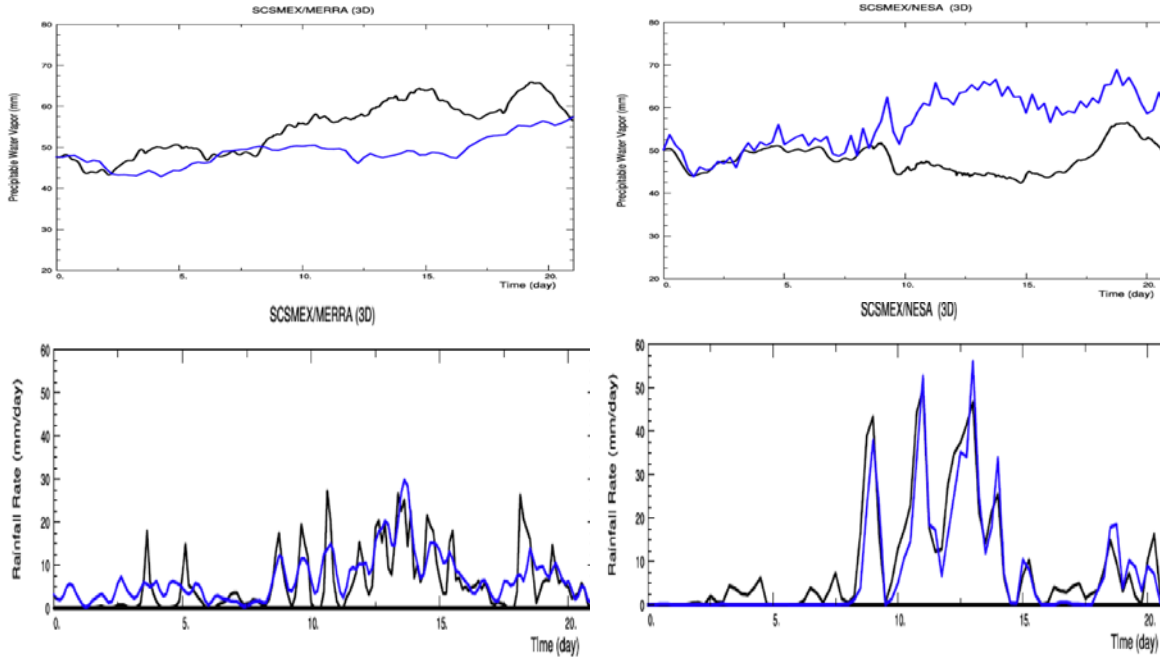


Fig. 22 Time series of simulated and observed precipitable water (upper panels) and precipitation rate (lower panels) using forcing derived from MERRA. The black lines are model-simulated, and the blue lines are observed. The left panels depict MERRA-forced simulations, and the right panels depict simulations using forcing derived from soundings during SCSMEX (NESA).